NASA Contractor Report 187084

Mixing and Non-Equilibrium Chemical Reaction in a Compressible Mixing Layer

Craig J. Steinberger
State University of New York at Buffalo
Buffalo, New York

May 1991

Prepared for
Lewis Research Center
Under Grant NAG3-1011

National Aeronautics and Space Administration

Abstract

The effects of compressibility, chemical reaction exothermicity and non-equilibrium chemical modeling in a reacting plane mixing layer were investigated by means of two dimensional direct numerical simulations. The chemical reaction was irreversible and second order of the type $A + B \rightarrow Products + Heat$. The general governing fluid equations of a compressible reacting flow field were solved by means of high order finite difference methods. Physical effects were then determined by examining the response of the mixing layer to variation of the relevant non-dimensionalized parameters.

The simulations show that increased compressibility generally results in a suppressed mixing, and consequently a reduced chemical reaction conversion rate. Reaction heat release was found to enhance mixing at the initial stages of the layer's growth, but had a stabilizing effect at later times. The increased stability manifested itself in the suppression or delay of the formation of large coherent structures within the flow.

Calculations were performed for a constant rate chemical kinetics model and an Arrhenius type kinetics prototype. The choice of the model was shown to have an effect on the development of the flow. The Arrhenius model caused a greater temperature increase due to reaction than the constant kinetics model. This had the same effect as increasing the exothermicity of the reaction. Localized flame quenching was also observed when the Zeldovich number was relatively large.

Acknowledgements

This work is sponsored by NASA Langley Research Center under Grant NAG 1-1122 and by NASA Lewis Research Center under Grant NAG 3-1011. Acknowledgement is also made to donors of the Petroleum Research Funds administered by the American Chemical Society for partial support of this work under Grant 22227-G6. All simulations were performed on Cray-2 and Cray YMP computers provided by NAS, NASA Langley and by the NCSA at the University of Illinois.

The author would like to thank Dr. Peyman Givi for his support, guidance, and advice in doing this work. The author is indebted to Drs. Phil Drummond and Mark Carpenter at NASA Langley Research Center, and to Dr. Cyrus Madnia for valuable discussions on the subject.

The efforts of all the members of the faculty the author has studied under in undergraduate and graduate school is gratefully appreciated.

Contents

List of Figures

Nomenclature

A_f : Arrhenius law constant

$\vec{b}_i$: body force for species i

c_p : specific heat at constant pressure

c_v : specific heat at constant volume

C : species concentration

C_e : heat release parameter

D : binary diffusion constant

Da : Damkohler number

D_T : thermal diffusion constant

E : total energy, activation energy

f_i : mass fraction for species i

$\mathbf{F}$: flux vector in the x direction

$\mathbf{G}$: flux vector in the y direction

h_i : enthalpy of species i

h_i° : reference enthalpy of species i

$\mathbf{H}$: source vector

ΔH° : heat of reaction

k : thermal conductivity

K_f : reaction rate constant

l_0 : physical length of computational domain

M_c : convective Mach number

N_s : number of species

p : pressure

Pr : Prandtl number

$\vec{q}$: heat flux vector

R : universal gas constant

$\mathbf{S}$,$\mathbf{T}$: numerically calculated derivatives

Sc : Schmidt number

t : time

t^* : normalized time

Δt : time step

T : Temperature

T_∞ : free stream temperature

u : streamwise velocity

$\tilde{u}_i$: streamwise diffusion velocity of species i

$\mathbf{U}$: dependent variable vector

U_∞ : free stream velocity

v : transverse velocity

$\tilde{v}_i$: transverse diffusion velocity of species i

$\tilde{V}_i$: diffusion velocity vector of species i

$\vec{V}$, $\mathbf{V}$: velocity vector

X_i : mole fraction of species i

$\dot{w}_i$: species production rate of species i

x : streamwise coordinate

Δx : streamwise spatial step size

y : transverse coordinate

Δy : transverse spatial step size

Ze : Zeldovich number

δ : Kronecker delta function

δ_ω : vorticity thickness

ϵ_1,ϵ_2 : amplitude of harmonic forcing

ρ : density

τ : shear stress

μ : laminar viscosity

φ : arbitrary transport variable

Subscripts:

A, B : chemical species

i, j : spatial indices

x : in x coordinate direction

y : in y coordinate direction

∞ : free stream

Chapter 1

Introduction

1.1 Motivation

Research on the subject of compressible reacting mixing layers has been of high priority in recent years [1]. Much of this effort has been devoted to the development of high speed air breathing flight vehicles. This type of vehicle would, according to current proposals, use a supersonic combustion ramjet (scramjet) engine. In such an engine, fuel is injected into a high speed airflow. The mechanisms of mixing and combustion of this non-premixed, high speed, compressible flow is of great complexity. In a simplistic approach, the problem may be divided into two parts: the effect hydrodynamic phenomena have on combustion, and the effect the combustion processes have on the hydrodynamics. Even divided as stated, the problem is still notoriously difficult. As such, only a few aspects of such phenomena and effects can be investigated in a single study.

In this investigation, it was intended to study some of the effects of coupling between mixing and reaction in compressible combusting systems. The system considered was a two-dimensional planar mixing layer, and a computational approach was chosen. The computational tool used was direct numerical simulation based on higher order finite difference algorithms. This method was chosen because of its free-

dom from turbulence modeling requirements (known also as a "model-free simulation" [2]), and its ability to compute the details of non-linear physical phenomena. The computational approach is suitable for use as a tool for basic research or as a compliment to experimental studies. The primary advantage of direct numerical simulation is the capability of evaluating all pertinent statistics of the flow without resorting to turbulence closure models. Simulations such as this usually require computational resources that were not readily available previously to researchers.

1.2 Previous Research

Given the extent of research on high speed mixing layers recently, it is not possible to include a comprehensive review of the accomplishments in this research area in this work. Thorough surveys of the state of the art have been performed by Givi and Riley [1], Givi [2], and Drummond [3], and will not be repeated here. Instead, a summary of some previous work will be presented, with priority given to those with direct relevance to the present effort. In particular, the scope of this review is limited to describing some of the recent accomplishments in investigations of the effects of compressibility on turbulence and large scale structures in parallel shear flows, and the influence of heat release and nonequilibrium chemical reactions on the development of these structures.

Brown and Roshko [4] found that the turbulent mixing layer is dominated by large scale coherent structures, or vortices. These structures convect at a nearly constant speed and tend to coalesce with neighboring vortices. The authors demonstrated that the reduction in mixing layer growth rate that had been observed in their experiments was due to the influence of compressibility effects, not density variations as had been thought previously. Ho and Huang [5] showed how the growth rate of the mixing layer could be manipulated by perturbing the flow at a subharmonic of the most amplified frequency. This technique stimulates the merging of the vortices, thus accelerating the

growth of the layer. A thorough review of the effects of harmonic forcing techniques is available in [6].

Papamoschou and Roshko [7] continued these experiments to examine the effect of compressibility on the spreading rate of a supersonic mixing layer. They found that it is useful to study the flow in a reference frame that travels with the flow at the same speed as an average large scale structure. A parameter which quantifies the compressibility in the flow was proposed as the convective Mach number, M_c; defined as the Mach number of the flow with respect to the above mentioned frame of reference. A direct correlation was found between M_c and the stability of the flow.

Ragab and Wu [8] substantiated the use of the convective Mach number as a relevant compressibility parameter by analyzing linear instability waves in supersonic shear layers. They also determined the stabilizing effect of the velocity and the temperature ratios between the two streams of the flow on the stability of the layer. It was found that there is a complex, non-linear relationship between the growth rate of the waves and the velocity ratio. It was also shown that at low Mach numbers, a temperature increase has a stabilizing effect, whereas at high Mach numbers the effect is to destabilize the flow. Lele [9] verified the results of Papamoschou and Roshko, by means of direct numerical simulation of a two-dimensional layer. He proposed an explanation of the compressibility stabilization effect based on the inviscid vorticity equation. Also, the development of eddy shocklets in the flow was noted for $M_c > 0.7$. These shocklets are formed as a result of locally supersonic regions that appear during vortex roll up or pairing, and remain attached to the vortices as the structures travel downstream. The effect of compressibility was further studied by Sandham and Reynolds [10] for both two and three dimensional mixing layers. The mixing layer growth rate was found to be reasonably predicted by linear stability analysis. Shocklets were captured in two-dimensional simulations when $M_c > 0.7$. It was also found that three-dimensional effects become significant at $M_c > 0.6$, and become dominant at $M_c > 1$. However, no eddy shocklets were observed in three-dimensional simula-

tions. Elliott and Samimy [11] performed experiments to investigate high Reynolds number compressible flows. They found a reduction in the level of turbulence fluctuations as the convective Mach number is increased.

The effects of an exothermic chemical reaction on fluid dynamics is another area of interest. Among recent computational efforts, McMurtry, *et al.* [12] performed direct numerical simulations of turbulent reacting mixing layers. They used an approximate set of equations that are valid for low Mach number flows. It was found that the heat liberated from a chemical reaction causes the layer to grow at a slower rate than that of a non-heat releasing flow. It was also shown that the magnitude of product formed and the amount of mass entrained into the vortical structures decrease as the intensity of heat release increases. These results agree with those obtained experimentally (e. g. [13]).

Jackson and Grosch [14] performed a linear stability analysis on supersonic reacting mixing layers. They found the existence of fast and slow stability modes, with the slow mode appearing only for flows with heat release. An increase in the amount of heat release was found to result in a reduction in the growth of the fast waves along with an increase in the growth of the slow waves. As the heat release is increased to large values, the slow mode becomes the most unstable. Thus, it was determined that the overall effect of increasing the heat release is to first stabilize the flow, then to destabilize it.

A direct numerical simulation of a supersonic reacting mixing layer was performed by Sekar, *et al.* [15]. They found reductions in the convective speed, the growth rate, and the entrainment of the free stream flows with increase in the magnitude of the heat release. They also found that the reduction of turbulence fluctuations with heat release occurs in supersonic flows to a lesser extent than that in incompressible flows. Their final conclusion was that heat release may not have a significant influence on the structure of the flow. Therefore, they suggest that for investigations concerned with mixing effects it might be useful to concentrate on phenomena related to gas-dynamic

effects rather than on exothermicity.

The phenomenon of flame extinction in non-premixed flames was the last area to be investigated. Although this has been the topic of theoretical and experimental study, direct numerical simulations of such flows have been somewhat limited. Recent reviews of some of the prevalent theories regarding the structure of turbulent non-premixed flames, as well as some of the experiments and numerical work in that field are provided by Bilger [16] and Peters [17]. A point that is made in these reviews is that although turbulent combustion modeling is very useful, there exists great uncertainty in the formulation of these models and in their use. This uncertainty is avoided by using "model free" simulations. Such simulations of non-premixed flames have been performed by Givi, *et al.* [18] and Givi and Jou [19]. However, these studies made certain limiting assumptions (i. e. constant density) that limit their applicability to low speed flows.

1.3 Scope of Present Research

The objective of this work is to examine the effects of compressibility and chemical reaction exothermicity on a reacting plane mixing layer. An examination is also made of the non-equilibrium effects of the chemical kinetics on the structure of a flame. These are accomplished by direct numerical simulation of an unsteady two dimensional layer. The governing equations are integrated via high order finite difference methods. Physical modeling is kept as simple as possible so that the physical effects described in the previous section can be isolated. This has an added advantage of saving considerable amounts of computational resources.

The mixing layer is assumed to be "temporally developing" with periodic boundary conditions. The fluid is assumed to be calorically perfect and to have constant and identical thermodynamic parameters. A simplified one step, second order irreversible reaction is used to describe the reactant conversion. Both constant rate and

Arrhenius type kinetics models are used. In most cases, the layer is perturbed only by numerical truncation and round off errors. For those cases where these are not sufficient to destabilize the flow, explicit harmonic forcing is added.

Physical effects are studied by changing the appropriate nondimensionalized parameters. Compressibility is represented by the convective Mach number, and reaction exothermicity is measured by the nondimensional value of the enthalpy of reaction. The chemical reaction is controlled by the magnitude of the Damkohler and the Zeldovich numbers.

The problem to be solved is formulated in Chapter 2, where the governing equations are presented and discretized into a vector form. The physical models used in the simulations are then presented, followed by a description of the numerical algorithms, and boundary conditions. Results from the simulations are presented in Chapter 3, where the effects of compressibility, reaction exothermicity and non-equilibrium chemistry are discussed. Finally, a summary, conclusions, and recommendations for future work are presented in Chapter 4.

Chapter 2

Numerical Formulation

2.1 Governing Equations

A two-dimensional compressible, reacting flow is governed by the continuity, momentum, energy, and species conservation equations coupled together with an equation of state. These are expressed as [20]:

Continuity

$$\frac{\partial \rho}{\partial t} + \nabla \cdot (\rho \vec{V}) = 0 \tag{2.1}$$

Momentum

$$\frac{\partial (\rho \vec{V})}{\partial t} + \nabla \cdot (\rho \vec{V} \vec{V}) = \nabla \cdot \tau + \rho \sum_{i=1}^{N_s} f_i \vec{b}_i \tag{2.2}$$

Energy

$$\frac{\partial (\rho E)}{\partial t} + \nabla \cdot (\rho \vec{V} E) = \nabla \cdot (\tau \cdot \vec{V}) - \nabla \cdot \vec{q} + \rho \sum_{i=1}^{N_s} f_i \vec{b}_i (\vec{V} + \vec{V}_i) \tag{2.3}$$

Species continuity

$$\frac{\partial (\rho f_i)}{\partial t} + \nabla \cdot (\rho \vec{V} f_i) = \dot{w}_i - \nabla \cdot (\rho f_i \vec{V}_i) \tag{2.4}$$

Equation of state

$$p = \rho R T \sum_{i=1}^{N_s} \frac{f_i}{M_i} \tag{2.5}$$

where

$$\tau \equiv \tau_{ij} = -\delta_{ij}p + \mu\left(\frac{\partial u_i}{\partial x_j} + \frac{\partial u_j}{\partial x_i}\right) + \delta_{ij}\lambda\frac{\partial u_k}{\partial x_k} \tag{2.6}$$

and

$$\vec{q} = -k\nabla T + \rho\sum_{i=1}^{N_s} h_i f_i \tilde{V}_i \tag{2.7}$$

The total energy is given by

$$E = \sum_{i=1}^{N_s} h_i f_i - \frac{p}{\rho} + \sum_{i=1}^{2}\frac{u_i^2}{2} \tag{2.8}$$

and the enthalpy of species i is defined as

$$h_i = h_i^\circ + \int_{T_r}^{T} c_{p_i} dT \qquad i = 1, 2, \ldots, N_s \tag{2.9}$$

2.2 Physical Modeling

This section discusses the various models needed to describe molecular diffusion and chemical reaction. For both processes it is possible to give complicated and computationally expensive models. However, to keep the computational cost at an affordable level, some simplifying assumptions are made. Since the goal of this research is to investigate the physics of reacting plane mixing layers in a general sense; models that are limited to specific reactions or particular species are not considered

It is assumed that the diffusivities of each chemical species are the same. Therefore, the diffusion of a species into another is proportional to respective concentration gradients. The effect of this is to decouple the equations for the diffusion velocities, and results in a form of Fick's law:

$$\tilde{V}_{i,j} = -\frac{D}{f_i}\frac{\partial f_i}{\partial x_j} \tag{2.10}$$

where $\tilde{V}_{i,j}$ is the diffusion velocity vector of the ith species in the jth coordinate

direction and D is the binary diffusion constant. The value of this constant is determined by choosing an appropriate value of the Schmidt number, Sc, since $D = \frac{\mu}{\rho Sc}$. Analogously, the mixture thermal conductivity is expressed by

$$k = \frac{c_p \mu}{Pr} \tag{2.11}$$

where Pr is the Prandtl number.

In earlier versions of the computational methodology used in this study [21] a diffusion model based on kinetic theory was used. In that model the diffusion velocities are described by the solution of an equation of the type:

$$\begin{aligned} \nabla X_i &= \sum_{j=1}^{N_s} \frac{X_i X_j}{D_{ij}} (\vec{V}_j - \vec{V}_i) + (f_i - X_i) \frac{\nabla p}{p} + \frac{\rho}{p} \sum_{j=1}^{N_s} f_i f_j (\vec{b}_i - \vec{b}_j) \\ &\quad + \sum_{j=1}^{N_s} \frac{X_i X_j}{\rho D_{ij}} \left(\frac{D_{Tj}}{f_j} - \frac{D_{Ti}}{f_i} \right) \frac{\nabla T}{T} \end{aligned} \tag{2.12}$$

The solution of Eq. (2.12) requires solving a system of N_s simultaneous equations, with N_s representing the total number of species involved in the reaction. This solution is computationally intensive and requires a coupled system of equations at each grid point throughout the computational domain. This process can require as much CPU time as solving the Navier-Stokes equations for the convective velocities [22].

In this work all of the species within the flow were given identical thermodynamic properties. Also, the assumption of a calorically perfect gas was made. All external body forces $\vec{b}_i$ were assumed to be negligible.

The chemical reaction in the flow is assumed to be of a simple, irreversible, second order type of the form

$$A + B \longrightarrow Product + Heat \tag{2.13}$$

The reaction is characterized by the kinetics mechanism, which is given by the single step model of

$$\dot{w} = K_f C_A C_B \tag{2.14}$$

where C_A and C_B represent the concentrations of the reacting species and are assumed equal at the free streams, i.e. $C_{A_\infty} = C_{B_\infty} = C_\infty$. K_f is the reaction rate constant, and can be normalized to form the definition of the Damkohler number, Da:

$$Da = \frac{K_f C_\infty}{U_\infty / \delta_\omega|_0} \tag{2.15}$$

In the present study two types of chemistry models were used; constant rate kinetics (i.e. constant K_f) and an Arrhenius type model in which K_f varies with the temperature. This is written as

$$K_f = A_f e^{-\frac{Ze}{T/T_\infty}} \tag{2.16}$$

where A_f is the pre-exponential factor and Ze is the Zeldovich number, defined as

$$Ze = \frac{E}{RT_\infty} \tag{2.17}$$

Here E is the activation energy and R is the universal gas constant. When the Arrhenius kinetic model is used, the pre-exponential factor A_f replaces K_f in the definition of Da (Eq. 2.15).

Combustion exothermicity is measured by the energy liberated by the chemical reaction, $\Delta H°$. The magnitude of this energy is parameterized by a non-dimensional heat release parameter Ce, defined by:

$$Ce = \frac{-\Delta H°}{c_v T_\infty} \tag{2.18}$$

Thus, $Ce = 0$ corresponds to a non-heat releasing chemical reaction.

2.3 Numerical Solution of the Governing Equations

The next step in the formulation is the discretization and the integration of Eqs. (2.1)–(2.4). In a vector form these equations are expressed by:

$$\frac{\partial \mathbf{U}}{\partial t} + \frac{\partial \mathbf{F}(U)}{\partial x} + \frac{\partial \mathbf{G}(U)}{\partial y} = \mathbf{H} \tag{2.19}$$

where **U** is the dependent variable vector,

$$\mathbf{U} = \left\{ \begin{array}{c} \rho \\ \rho u \\ \rho v \\ \rho E \\ \rho f_i \end{array} \right\} \tag{2.20}$$

F and **G** contain the diffusive and convective flux vectors in the x and y directions respectively,

$$\mathbf{F} = \left\{ \begin{array}{c} \rho u \\ \rho u u - \sigma_x \\ \rho u v - \tau_{yx} \\ (\rho E - \sigma_x)\, u - \tau_{xy} v + q_x \\ \rho u f_i + \rho \tilde{u}_i f_i \end{array} \right\} \tag{2.21}$$

and

$$\mathbf{G} = \left\{ \begin{array}{c} \rho v \\ \rho u v - \tau_{xy} \\ \rho v v - \sigma_y \\ (\rho E - \sigma_y) v - \tau_{yx} u + q_y \\ \rho v f_i + \rho \tilde{v}_i f_i \end{array} \right\} \tag{2.22}$$

$\sigma_x = \tau_{xx}$ and $\sigma_y = \tau_{yy}$. Finally, $\mathbf{H}$ is the source vector:

$$\mathbf{H} = \begin{Bmatrix} 0 \\ \rho \sum_i f_i b_{ix} \\ \rho \sum_i f_i b_{iy} \\ \rho \sum_i f_i \mathbf{b}_i (\mathbf{V} + \tilde{\mathbf{V}}) \\ \dot{w}_i \end{Bmatrix} \tag{2.23}$$

For the purpose of numerical discretization, it is convenient to map these equations from the physical domain into an appropriate computational space. In the simulations performed here the grids are highly compressed in the transverse direction of the flow, with maximum compression along the region of maximum shear. This compression provides a sufficiently fine resolution in the area of large velocity and concentration gradients. A detailed explanation of the grid generation routine and the transformation process may be found in [21].

Two numerical schemes were utilized to integrate the governing equations; an algorithm proposed by Gottlieb and Turkel [23] and a compact parameter scheme developed by Carpenter [24]. Both methods are second order accurate in time and fourth order accurate in space. The two algorithms are dissipative, allowing a more accurate treatment of sharp gradients compared with non-dissipative methods. The main advantage of these methods is their capability in capturing shocks and reaction zones.

The Gottlieb-Turkel scheme is a variant of the well known MacCormack predictor-corrector method [25]. For Eq. (2.19), it is implemented as:
Predictor:

$$\mathbf{U}^*_{i,j} = \mathbf{U}^n_{i,j} - \frac{\lambda_x}{6}\left[-\mathbf{F}^n_{i+2,j} + 8\mathbf{F}^n_{i+1,j} - 7\mathbf{F}^n_{i,j}\right] - \frac{\lambda_y}{6}\left[-\mathbf{G}^n_{i,j+2} + 8\mathbf{G}^n_{i,j+1} - 7\mathbf{G}^n_{i,j}\right] + \Delta t \mathbf{H}^n_{i,j} \tag{2.24}$$

Corrector:

$$\mathbf{U}^{**}_{i,j} = \mathbf{U}^{*}_{i,j} - \frac{\lambda_x}{6}\left[7\mathbf{F}^{*}_{i,j} - 8\mathbf{F}^{*}_{i-1,j} + \mathbf{F}^{*}_{i-2,j}\right] - \frac{\lambda_y}{6}\left[7\mathbf{G}^{*}_{i,j} - 8\mathbf{G}^{*}_{i,j-1} + \mathbf{G}^{*}_{i,j-2}\right] + \Delta t\mathbf{H}^{*}_{i,j} \tag{2.25}$$

$$\mathbf{U}^{n+1}_{i,j} = \frac{1}{2}\left[\mathbf{U}^{n}_{i,j} + \mathbf{U}^{**}_{i,j}\right] \tag{2.26}$$

where $\lambda_x = \frac{\Delta t}{\Delta x}$ and $\lambda_y = \frac{\Delta t}{\Delta y}$. The CFL ($\lambda_x$ or λ_y) condition for stability requires CFL $\leq \frac{2}{3}$. A disadvantage of the method is the need for a use of a five point stencil, thus precluding its use on the gridpoints next to the boundaries of the computational domain. For this reason, and in an effort to improve the accuracy, a family of dissipative compact parameter schemes (DCPS) are also considered. For Eq. (2.19), the DCPS takes the form of:

Predictor:

$$D\mathbf{S}^{n}_{i-1,j} + \mathbf{S}^{n}_{i,j} + D\mathbf{S}^{n}_{i+1,j} = \frac{(B-A)\mathbf{F}^{n}_{i-1,j} + C\mathbf{F}^{n}_{i,j} + (B+A)\mathbf{F}^{n}_{i+1,j}}{\Delta x} \tag{2.27}$$

$$D\mathbf{T}^{n}_{i,j-1} + \mathbf{T}^{n}_{i,j} + D\mathbf{T}^{n}_{i,j+1} = \frac{(B-A)\mathbf{G}^{n}_{i,j-1} + C\mathbf{G}^{n}_{i,j} + (B+A)\mathbf{G}^{n}_{i,j+1}}{\Delta y} \tag{2.28}$$

$$\mathbf{U}^{*}_{i,j} = \mathbf{U}^{n}_{i,j} - \Delta t(\mathbf{S}^{n}_{i,j} + \mathbf{T}^{n}_{i,j} - \mathbf{H}^{n}_{i,j}) \tag{2.29}$$

Corrector:

$$D\mathbf{S}^{*}_{i-1,j} + \mathbf{S}^{*}_{i,j} + D\mathbf{S}^{*}_{i+1,j} = \frac{-(B+A)\mathbf{F}^{*}_{i-1,j} - C\mathbf{F}^{*}_{i,j} - (B-A)\mathbf{F}^{*}_{i+1,j}}{\Delta x} \tag{2.30}$$

$$D\mathbf{T}^{*}_{i,j-1} + \mathbf{T}^{*}_{i,j} + D\mathbf{T}^{*}_{i,j+1} = \frac{-(B+A)\mathbf{G}^{*}_{i,j-1} - C\mathbf{G}^{*}_{i,j} - (B-A)\mathbf{G}^{*}_{i,j+1}}{\Delta y} \tag{2.31}$$

$$\mathbf{U}^{**}_{i,j} = \mathbf{U}^{*}_{i,j} - \Delta t(\mathbf{S}^{*}_{i,j} + \mathbf{T}^{*}_{i,j} - \mathbf{H}^{*}_{i,j}) \tag{2.32}$$

$$\mathbf{U}^{n+1}_{i,j} = \frac{1}{2}\left[\mathbf{U}^{n}_{i,j} + \mathbf{U}^{**}_{i,j}\right] \tag{2.33}$$

In Eqs. (2.27)-(2.32) $A = \frac{3}{4}$, $C = -2B$, and $D = \frac{1}{4}$ [24]. $\mathbf{S}^{n}_{i,j}$ and $\mathbf{S}^{*}_{i,j}$ are the numerical values of the derivative of $\mathbf{F}$, and $\mathbf{T}^{n}_{i,j}$ and $\mathbf{T}^{*}_{i,j}$ are the numerical values of the

derivative of **G**. **S** and **T** must be calculated implicitly at each of the predictor and corrector stages by inverting a tri-diagonal matrix. If a flow with periodic boundary conditions are considered, a periodic tri-diagonal matrix must be inverted. This represents a one parameter family of methods in B. The value of B at which the maximum allowable CFL occurs is $B = \frac{\sqrt{3}}{4}$. The CFL condition in this case is $\frac{1}{2}$. To preserve $(\Delta t^2, \Delta x^4, \Delta y^4)$ accuracy, the predictor-corrector sequence must be switched at each time step (i.e. Forward/Forward-Backward/Backward, then Backward/Backward-Forward/Forward). This cycling procedure has an added advantage of dampening an instability that may occur when either scheme is formulated in two (or more) dimensions.

The advantages of these higher order algorithms in comparison with some of the conventionally utilized lower order difference methods were demonstrated by comparing results generated by all these schemes to the results of some test problems with known analytical solutions. The lower order discretization schemes are based on a first order upwinding method [26] and the second order MacCormack scheme [25] In this demonstration, a linear wave equation was considered, and comparisons were made for both one and two-dimensional cases. In the former, the linear advection of a square wave concentration distribution was considered, and in the latter the solid body rotation of a sharp gradient scalar field was investigated. With the absence of diffusion, the scalar field retains its initial shape in both cases; providing an effective means of evaluating the discretization routines.

The results indicated that the Gottlieb-Turkel method and the DCPS provide a substantial improvement over the first order upwind and second order MacCormack schemes in that the magnitudes of both the truncation and the phase errors are substantially reduced. Also, the DCPS method resulted in slightly lower phase error than generated by the Gottlieb-Turkel scheme. However, the computational requirements for the DCPS was about 25% more than that required by the Gottlieb-Turkel algorithm. Similar tests were previously performed by Carpenter [24], who utilized the

MacCormack, Gottlieb-Turkel, and DCPS methods to calculate the growth rates and the characteristic frequencies for a temporally developing compressible mixing layer, and compared the results to those given by a spectral linear stability method. In this comparison, the DCPS was found to be twice as accurate as the MacCormack and the Gottlieb-Turkel methods.

In view of these comparisons, it was decided to select the Gottlieb-Turkel and DCPS algorithms in favor of other alternatives. This decision was made mainly to keep the numerical truncation errors at most of order $O(\Delta t^2,\ \Delta x^4,\ \Delta y^4)$. In the subsequent chapters, both of these methods are used interchangeably with consideration to available computational resources. However, only one method was used to describe each physical phenomenon. Namely, the Gottlieb-Turkel method was used in the calculations discussed in Sections 3.1 and 3.2, whereas the DCPS was used in those presented in Section 3.3.

2.4 Initial and Boundary Conditions

One of the primary assumptions made in these simulations is that the mixing layer is temporally developing. That is, the reference frame of the simulations is defined to be traveling along with the average velocity of the flow. The advantages of this approximation are twofold. First, with the temporal assumption the inflow and outflow boundary conditions can be assumed periodic. This removes the difficult problem of specifying the boundary conditions. Second, the temporal assumption means that only a relatively small region of the flow is being simulated. This region is then followed in a Lagrangian sense as time progresses. This results in considerable computational savings, namely in CPU time and memory allocation. These savings can then be used to simulate the flow in a greater detail. The primary disadvantage of a temporal approximation is that asymmetric effects in the flow can not be captured [27]. These effects are not significant in the scope of the present research.

A representation of the initial flow field is shown in Fig. 1. The flow on the top stream moves towards the right with a free-stream streamwise velocity of U_∞, and the bottom stream moves to the left with the same speed ($-U_\infty$). The flowfield is initialized with a hyperbolic tangent streamwise velocity profile with a specified initial vorticity thickness ($\delta_\omega|_0$). There is no initial fluid motion in the transverse (Y) direction. The pressure was initially assumed to be constant throughout the flow field. Depending on the problem simulated, the temperature was either assumed to be initially constant or had an initial distribution of the form:

$$T = T_\infty(1 + 4e^{-1000y^*}) \tag{2.34}$$

where y^* is the normalized spatial coordinate in the transverse direction, defined as $y^* = (y - 0.5y_{max})/y_{max}$. Reactant A covers the top half of the physical domain, and reactant B covers the bottom half. It was assumed that the upper and lower walls were far enough away from the mixing layer that free stream conditions could be imposed.

In most cases, no explicit forcing was added to the base flow. The simulations relied on numerical truncation errors to provide perturbations to the layer to trigger formation of coherent vortices. For most cases, this was sufficient. However, in some cases where the physical effects had a stabilizing effect on the flow, harmonic forcing was explicitly added. The forcing used was that determined by a linear stability analysis of a temporally developing incompressible layer with the same initial velocity distribution as that employed here [28]. No attempts were made to find the most unstable modes for the compressible flow. This is justified in view of the fact that the study is focused on investigating the effects of large scale structures once they are formed, not how these structures are most rapidly generated.

Chapter 3

Presentation of Results

The results of the numerical simulations will be presented in three forms: integral or global representations, statistical sampling, and flow visualization. A global representation of how the state of the flow changes with time is given by considering the temporal variation of integral parameters, for example the vorticity thickness or the total amount of product formed. The second form of presentation of result is performed by examining the cross-stream variations of the statistics of the relevant variables. With the approximation of temporal evolution, the flow is considered homogeneous in the streamwise direction X, and the statistical information is obtained by sampling the data in this direction. In this way, the ensemble mean and mean square of an arbitrary transport variable φ are obtained by

$$\langle \varphi(Y) \rangle = \frac{1}{N} \sum_{i=1}^{N} \varphi_i(Y) \tag{3.1}$$

$$\left\langle \varphi'^2(Y) \right\rangle = \frac{1}{N} \sum_{i=1}^{N} (\varphi_i - \langle \varphi \rangle)^2 \tag{3.2}$$

where $\langle\ \rangle$ denotes an ensemble average, the subscript i indicates the grid index, and N is the total number of grid points in the X direction.

The final method of result presentation, flow visualization, is provided by present-

ing the data in the form of contour plots. This type of presentation is an effective method of visualizing the flow. A typical contour plot of the vorticity is shown in Fig. 2. This figure shows that the computational grid is compressed in the transverse direction, with maximum compression occurring along the centerline of the vortex. Only a magnified portion of the entire computational grid is presented in this figure to highlight the details. All of the contour plots that follow will be presented on a uniform, or physical grid. The fluctuations near the outer portions of the figure may be attributed to numerical noise. Although the amplitude of the fluctuations is small compared to the physical values, they are still displayed due to deficiencies in the graphics software used.

All parameters are normalized when appropriate by initial or free stream conditions. Time is normalized by

$$t^* = \frac{t}{l_0/U_\infty} \tag{3.3}$$

where l_0 is the physical size of the computational box.

3.1 Compressibility Effects

The effect of compressibility on a mixing layer was studied by varying the convective Mach number, M_c, while keeping all other parameters constant in a non-reacting layer. The flow was examined for M_c = 0.2, 0.4, 0.8, and 1.2. The grid resolution of the M_c = 0.2 case consisted of 127 × 127 grid points, and for the other cases it consisted of 256 × 256 grid points. The increased resolution was necessary to resolve the strong gradients that exist at high compressibility. No explicit forcing was added to the flow. The vorticity thickness vs. normalized time for different values of M_c is given in Fig. 3. This figure shows that the growth rate of the vorticity thickness is clearly decreased with increased compressibility. Compressibility also affects the time needed for the layer to roll up into a vortex. The onset of roll-up is signified by a large jump in the vorticity thickness. The compressibility also affects the size of the

vortex formed, with the thickness of $M_c = 0.2$ layer being about 50% larger than the $M_c = 0.8$ vortex.

The profiles of the normalized average streamwise component of the velocity is shown in Figs. 4–6. The most significant feature portrayed by these figures is the steepness of the mean velocity profiles at high convective Mach numbers. This shows a sharper velocity gradient across the layer, implying a lesser rate of mixing. As time progresses, the slopes of the profiles begin to decrease. The suppression of turbulence fluctuations with compressibility is shown by the profiles of the mean square of the fluctuating velocity. The transverse variation of the fluctuation is shown in Fig. 7 for time $t^* = 6$ and in Fig. 8 for time $t^* = 8$. A marked decrease in the amplitude of the fluctuations can easily be observed. For $t^* = 6$, the fluctuations for the higher compressibility cases are almost negligible compared to those at low compressibility. At $t^* = 8$, the fluctuations for $M_c = 0.8$ and $M_c = 1.2$ are evident, although at lower amplitudes than those in lower compressibility cases. The reduction of turbulence fluctuations is further illustrated in Figs. 9 and 10, which show Reynolds stress profiles in the mixing layer at times $t^* = 6$ and $t^* = 8$.

The pressure response for the layer to the formation of large scale structures is shown in Figs. 11 through 16 for $M_c = 0.2$ through $M_c = 1.2$. The regions of pressure minima occur at the location of vortex cores. Similarly, pressure minima are located at the braids between the large scale structures, at the point of minimum vorticity. This is evident by a comparison between Figs. 11 and 25. Another interesting feature of the increased compressibility is shown by examining the plots of pressure contours at high convective Mach numbers, shown in Figs. 12–16. In these cases, the increased compressibility results in steep pressure gradients and in the creation of "eddy shocklets." These shocklets are initiated at the shear zone of the layer, and extend to the outer region of the flow near the boundaries. The layer is dominated by regions of locally subsonic and supersonic flow. To adjust to the pressure differences between these regions, a shocklet, albeit a weak one, is created. Further examination

shows that the regions of high compressibility tend to push the shocklets backwards in the opposite direction of the motion of the large scale structures. Therefore, the shocklets rotate in a direction opposite to the rotation of the large scale vortices. Contours of the instantaneous Mach number show that the shocklets are related to the formation of large scale vortical structures, illustrated in Figs. 17 through 20. The form of these structures, as well as localized regions of subsonic and supersonic flow are clearly seen. Examination of the instantaneous Mach number contours indicates that the strength of the shocks increase with the increase of the convective Mach number.

The appearance of shocklets in flows of $M_c > 0.7$ has been previously reported by Lele [9] and by Sandham and Reynolds [10] for two dimensional simulations. This phenomenon has not been observed in experimental studies, nor has it been reported in existing three dimensional mixing layer simulations. Shocklets have also been noted in simulations of homogeneous turbulence [29]. It has been suggested [30] that the appearance and strength of shocklets within the flow might be predicted by examining the root mean square of the Mach number and the normalized root mean square of the density. For example, the ratio of the two parameters may be defined as

$$\alpha = \frac{\sqrt{\overline{M'^2}}}{\sqrt{\overline{\rho'^2}}/\rho_\infty} \tag{3.4}$$

For $M_\infty \approx O(1)$, if $\alpha > 1$ the flow would be quasi-incompressible, i. e. no shocklets would appear. However, shocklets would appear for $\alpha < 1$. Profiles of α are shown in Fig. 21 for $M_c = 0.2$ and in Fig. 22 for $M_c = 0.8$. The figures show that $\alpha > 1$ for all y^* when $M_c = 0.2$, and $\alpha < 1$ at some locations for $M_c = 0.8$. Shocklets appear for $M_c = 0.8$, but not for $M_c = 0.2$. This indicates some correlation between the order of ratio of the root mean squares of the Mach number and density and the appearance of shocklets in the flow. However, more work is clearly needed.

3.2 Effects of Reaction Exothermicity

The effects of an exothermic chemical reaction can be depicted by repeating the procedure above for varying values of the heat release parameter, C_e, while keeping other parameters constant. Results are presented for constant rate kinetics with heat release values of $C_e = 0, 1.5$, and 6; and for Arrhenius type kinetics with $Ce = 1.5$ and $Ze = 10$. In these simulations, a grid of 127×127 points was used, the Damkohler number was set equal to 10, and M_c was set equal to 0.2. No harmonic forcing was added.

The results of these simulations are first presented in the form of plots of the vorticity thickness versus normalized time for all four cases (Fig. 23). This figure shows that the rate of growth is highest for the non-heat releasing case ($C_e = 0$), and as the heat release parameter is increased, the coupling between the reaction and the hydrodynamics causes the layer to grow at a lower rate. The relatively smooth regions of the vorticity thickness growth may be attributed to diffusion thickening and a jump in magnitude of this thickness represents vortex roll-up. For the $C_e = 0$ case, the layer responds to perturbations fairly quickly, and vortical structures are formed at $t^* \approx 3$. An increase in the magnitude of the heat release results in a delay of vortex roll-up, and the jump in vorticity thickness does not occur until $t^* \approx 7$. Further increase in the magnitude of the heat release results in additional delays, as can be seen from the case of $C_e = 6$. This is also observed for the Arrhenius model with $C_e = 1.5$. In these two cases, the effects of exothermicity is most pronounced; vorticity roll-up does not occur at all, and the only growth in the thickness of the mixing layer is due to molecular diffusion.

The vorticity contour plots demonstrate this point further. These are shown in Figs. 24 through 33 for each value of the heat release parameter at various times. As mentioned above, the non-heat releasing layer goes through roll-up and pairing fairly quickly (Figs. 24–26). The resulting large scale structure then rotates clockwise as time progresses. After the collapse of the vortex, no additional roll-up occurs, causing

a fluctuation in the magnitude of the vorticity thicknesses as shown in Fig. 23. The vorticity contours of the $C_e = 1.5$ and constant chemical kinetics case for several times are presented in Figs. 27–29 . At time $t^* = 6$, when the non-heat releasing layer has already rolled up, this mixing layer is only showing the initial stages of instability. When the large scale structures are finally formed, the vorticity thickness of the layer has grown via diffusion to twice that of the non-heat releasing case right before the roll-up. As in the previous case, there are two distinct structures in the flow which combine into one. This is not apparent from the vorticity thickness profile, since the initial pairing is masked by the size of the shear layer. Further increase in the heat release prevent the mixing layer from responding to background perturbations at all. The contour plots of the vorticity in both cases, shown for $t^* = 8$ in Figs. 31 and 33, are composed of parallel lines, which indicate the lack of formation of any vortical structures. At larger times, the layer becomes too "thick" to respond to the background perturbations, and procceding in time does not produce any substantial enhancement in mixing except that facilitated by diffusion. The mixing rate in the reacting layer with the Arrhenius model is severely retarded compared to that of the constant kinetics case. With the application of the Arrhenius reaction model, the rate of increase of temperature is substantially more than that of the constant rate kinetics model, even though the heat release parameter is kept fixed. This increase in the local and the global magnitudes of the temperature stabilizes the flow, and for the case of $Ze = 10$, the instability modes in the layer do not seem to grow fast enough to form large scale coherent vortices.

The influence of the heat release on the structure of the flame is demonstrated by examining the product thickness of the layer, defined by the normalized total product concentration of the layer as a function of time (Fig. 34). An examination of this figure shows the influence of heat release on all stages of the development of the layer. At initial times, the effect of heat release is an enhanced product formation, while the reverse applies at the intermediate and final stages. Initially, the effect of heat release

is to expand the fluid at the cores of the layer. A large mixing zone is formed, which results in an enhanced reaction and an increased product formation. This explains the increased thickness at initial times. However, as the heat release increases and the layer thickens, the growth of the instability modes become subdued, postponing the formation of large scale vortices. After initial times, the non-heat release ($C_e = 0$) and $C_e = 1.5$ cases predict a sharp increase in the product thickness. This is caused by the dynamics of the large scale structure formation. The mechanism of roll-up causes the reactants to be entrained into the layer from their respective free streams. This produces an increase in the extent of mixing, reaction and product formations. The lack of roll-up in the $C_e = 6$ and Arrhenius cases means the only mixing mechanism is due to molecular diffusion. Since in these simulations the diffusion mechanism is not as efficient as the roll-up of vortices in mixing reactants, the product thickness is correspondingly lower.

Further influences of heat release become apparent by examining the effect on statistical quantities. In Figs. 35 through 37, the normalized profiles of the mean streamwise velocity component are presented at three different times. At early times, the gradients of the velocity for the low heat release cases are steeper than that of the higher heat release cases. This is caused by the local expansion of fluid inside the core of the layer. At later times the high heat release cases have a higher profile gradient, and thus, less mixing. This has a substantial influence on the two-dimensional turbulence transport, as indicated by the cross-stream variations of the streamwise velocity mean square, presented in Figs. 38 through 40. These figures show how the amplitude of the fluctuations decrease when the heat release is increased. Similar trends are observed in the profiles of the Reynolds stress shown in Figs. 41 through 43 for three different times. The heat release clearly has a stabilizing effect on the flow, demonstrated by the reduction of the turbulent fluctuations.

The results of these simulations are consistent with the linear stability analysis of a stratified mixing layer, in that the density reduction in the middle region of the layer

has a stabilizing effect [31]. However, this analysis was presented for a non-reacting layer. The effects of chemical reaction on linear stability is currently being studied by Hu and Givi [32].

3.3 Flame Extinction

The nonequilibrium effects leading to local flame extinction in the reacting mixing layer was the final topic of this investigation. Simulations were performed using an Arrhenius chemical kinetics model, and repeated under otherwise identical conditions using constant rate kinetics for comparison. The Zeldovich number was chosen as 20, the Damkohler number was set to 10, the convective Mach number was set equal to 0.2, and the heat release parameter was set at 1.5. A grid of 127 $\times$ 127 points was used. The temperature field was initialized with a Gaussian distribution in the transverse direction and a constant distribution in the streamwise direction. The maximum temperature occurred along the centerline of the layer and had a value of five times the free stream temperature.

The initial temperature distribution has a stabilizing effect on the flow. In order to trigger the formation of large scale structures, explicit harmonic forcing was added. The effects of three initial perturbation mechanisms were examined. These were: case I, the most unstable mode was added to the initial velocity profile, case II, the most unstable mode plus its first subharmonic were added, and lastly a control case with no forcing. The amplitude of the forcing, ϵ_1 for the most unstable mode, and ϵ_2 for the first subharmonic of the most unstable mode, were set to 0.5% of the mean flow. For the purpose of evaluating the effects of harmonic forcing, the Damkohler number was set to zero.

The influence forcing has on the development of the vorticity thickness is shown in Fig. 44. As expected, the non-forced layer remains stable and only grows via molecular diffusion. The forced cases appear to have identical growth until time $t^* \approx 1$. At this

time, the growth of the layers follow different paths, with the case I layer growing to about twice the thickness of the case II and non-forced layers. This is explained by presenting the vorticity contours for three points in time; $t^* = 1$, right before the layers diverge, $t^* = 1.5$, soon after the split, and $t^* = 2.1$, at a time later than the divergence. For the unforced case, the vorticity is shown as parallel lines; there is no significant instability within flow (Figs. 45 and 46). As time progresses, the layer thickens via molecular diffusion until there is no possibility for the background perturbations to grow. At $t^* = 1$, the forced layers, shown in Figs. 47 and 50, have both rolled up into a pair of vortices. It can be seen in Fig. 48 that at $t^* = 1.5$, the case I vortices have elongated slightly and have taken on an elliptical shape. In case II, the addition of the first subharmonic initiates a second roll-up (Fig. 51) resulting in a pairing of the vortices. At time $t^* = 2.1$ the case I layer, shown in Fig. 49, has taken an even more exaggerated elliptical shape than that at the previous time. The case II flow has paired into a single coherent structure shown in Fig. 52. In the center of the structure, the cores of the previous vortices may still be seen.

After the examinations of the effects of harmonic forcing, simulations were then performed for the Arrhenius and constant rate kinetics models. Since the most pronounced mixing is desired, perturbations associated with the most unstable mode plus the first subharmonic were used in these simulations. Contour plots of the instantaneous reaction rate and the product concentrations may be examined to provide insight into the progress and the structure of the reaction. These contours are shown in Figs. 53 and 54 for time $t^* = 1$, when the vortices have just been formed. Note the high concentrations of product in the core of the vortices where the most mixing occurs. The reaction rate is highest along the mixing surface of the layer, that is, in the center of the intervortex braids. The contours at $t^* = 1.5$ (presented in Figs. 55 and 56) portray the behavior at the initial stages of pairing. The reaction rate has begun to decrease in the braids of the emerged vortex. At time $t^* = 2.25$, shown in Figs. 57 and 58, the layer has completed the pairing process and strong gradients are

observed in the vortex braids. Since the braids are "stretched " as the vortex rotates, they are the area of the highest strain. The flame at the onset of extinction is shown in Figs. 59 and 60. Note that the reaction rate has gone to zero at the braids. The product concentration contour shows that no product exists in these extinguished regions. This demonstrates that the flame did not quench due to depletion of reactants. At this point in time, the flame is not continuous, forming what will be called for lack of a better term, a "flame eddy."

This extinction phenomenon has been explained by Peters [33] as follows: At the regions of high strain, the reactants are supplied at a faster rate than they can be consumed by the flame. Thus the local temperature in that area drops and the flame becomes very rich with the reactants. As a result, the flame is quenched in that area. If a fast chemistry model or an equilibrium chemistry model is used, the extinction mechanism can not be captured. Investigation of such phenomena requires finite-rate chemistry simulation in the form presented here.

Chapter 4

Summary and Conclusions

This work deals with direct numerical simulation of a compressible, temporally developing, reacting plane mixing layer. Several simplifying approximations were made so that the effects of the variation of isolated parameters could be studied in detail. In particular, the chemical reaction was assumed to be of the type $A + B \longrightarrow Products + Heat$, and thermodynamic properties were assumed constant and identical for all the species. Two types of kinetics models were used, one with constant rate kinetics, and another with an Arrhenius model. In the constant rate case, the Damkohler number was the parameter that described the reaction, while both the Damkohler number and the Zeldovich number were used to describe the Arrhenius reactions. A simple linear gradient model was employed to model all the diffusion processes. Integration of the governing transport equations was performed by higher order finite difference methods. The two methods used here were the Gottlieb-Turkel two-four dissipative scheme and Carpenter's dissipative compact parameter scheme (DCPS). The results obtained were not affected significantly by the choice of numerical algorithm.

Studies of various flow phenomena were performed by varying one representative nondimensionalized parameter while keeping all other parameters constant. The convective Mach number, M_c, was used to describe compressibility, the heat release

parameter, C_e, represented the exothermicity of the reaction, and the Damkohler number and the Zeldovich number quantified the extent of the reaction.

The simulations concerning the effect of compressibility on the mixing layer showed a direct correlation between increased compressibility, increased stability, and reduced turbulence. When the convective Mach number was increased, the rate of growth of the mixing layer, which was measured by the growth of the vorticity thickness, was markedly reduced. Degradation of the development of the streamwise fluctuating velocity and the Reynolds stress profiles was also noted. For high compressibility cases, eddy shocklets were observed within the flow. This has been reported in some previous two dimensional simulations, but has not been observed in experiments or in three dimensional simulations. An expansion of this problem into three dimensions is suggested for future work in this area.

Increased exothermicity was observed to slow the growth of large scale structures. At the initial stages of development, high heat release increased the amount of product formed via volumetric expansion of the core of the layer. However, the heat release caused the layer to be less responsive to perturbations, reducing the growth of the layer at later stages. The overall effect of increased heat release, therefore, was to stabilize the flow and to decrease the extent of reaction. This was shown by examining the contour plots of selected quantities as well as statistical variations of those quantities.

The selection of chemical kinetics model was shown to have significant effect on the development of the flow. The introduction of an Arrhenius chemistry model had a stabilizing effect, thus degrading the progress of the reaction. When the layer was harmonically forced, the structure of the flow was found to be controllable by varying the type of perturbation. When only the most unstable frequency of the layer was added to the mean flow, the layer went through a single roll-up process. The inclusion of the first subharmonic of that frequency caused the layer to go through a second roll-up, in the form of pairing of the neighboring vortices. Non-equilibrium effects of

the kinetics model was studied for the last case. It was found that at high Zeldovich numbers, the flame would be quenched at regions with large local values of the strain rates. Suggestions for future work in this aspect of research include extending the simulations to three dimensions and adding more realistic chemistry models.

References

[1] P. Givi and J. J. Riley, "Some current issues in the analysis of reacting shear layers: Computational challenges," in *Proceedings of Combustion Workshop* (R. Voist, M. Y. Hussani, and A. Kumar, eds.), (Hampton, VA), Springer-Verlag, October 1990.

[2] P. Givi, "Model free simulations of turbulent reactive flows," *Prog. Energy Comb. Science*, vol. 15, no. 1, pp. 1–107, 1989.

[3] J. P. Drummond, "Supersonic reacting internal flow fields," in *Numerical Approaches in Combustion Modeling* (E. S. Oran and J. P. Boris, eds.), AIAA Progress in Aeronautics and Astronautics, 1990. in press.

[4] G. L. Brown and A. Roshko, "On density effects and large structure in turbulent mixing layers," *J. Fluid Mech.*, vol. 64, pp. 775–816, 1974.

[5] C.-M. Ho and L.-S. Huang, "Subharmonics and vortex merging in mixing layers," *J. Fluid Mech.*, vol. 119, pp. 443–473, 1982.

[6] C.-M. Ho and P. Huerre, "Perturbed free shear layers," *Ann. Rev. Fluid Mech.*, vol. 16, 1984.

[7] D. Papamoschou and A. Roshko, "Observations of supersonic free shear layers," AIAA Paper 86-0162, 24th Aerospace Sciences Meeting, Reno, Nevada, January 1986.

[8] S. A. Ragab and J. L. Wu, "Linear instabilities in two dimensional compressible mixing layers," *Phys. Fluids A*, vol. 1, pp. 957–966, June 1989.

[9] S. K. Lele, "Direct numerical simulation of compressible free shear flows," AIAA Paper 89-0374, 27th Aerospace Sciences Meeting, Reno, Nevada, January 1989.

[10] N. D. Sandham and W. C. Reynolds, "A numerical investigation of the compressible mixing layer," Report No. TF-45, Stanford University, Department of Mechanical Engineering, Thermosciences Division, September 1989.

[11] G. Elliott and M. Samimy, "Compressibility effects in free shear layers," AIAA Paper 90-0705, 28th Aerospace Sciences Meeting, Reno, Nevada, January 1990.

[12] P. A. McMurtry, J. J. Riley, and R. W. Metcalfe, "Effects of heat release on the large scale structures in a turbulent reacting mixing layer," *J. Fluid Mech.*, vol. 199, pp. 297–332, 1989.

[13] J. C. Hermanson and P. E. Dimotakis, "Effects of heat release in turbulent, reacting shear layer," *J. Fluid Mech.*, vol. 199, pp. 333–375, 1989.

[14] T. L. Jackson and C. E. Grosch, "Effect of heat release on the spatial stability of a supersonic reacting mixing layer," ICASE Report No. 88-68, Institute for Computer Applications in Science and Engineering, NASA Langley Research Center, Hampton Va., November 1988. Also available as NASA CR 181753.

[15] B. Sekar, H. S. Mukunda, and M. H. Carpenter, "The direct simulation of high speed mixing layers without and with chemical heat release," in *Proceedings of CFD Symposium on Aeropropulsion*, (Cleveland, OH), April 1990.

[16] R. W. Bilger, "Turbulent diffusion flames," *Ann. Rev. Fluid Mech.*, vol. 21, pp. 101–135, 1989.

[17] N. Peters, "Laminar flamelet concepts in turbulent combustion," in *Proceedings of the Twenty-first Symposium (Int.) on Combustion*, pp. 1231–1250, The Combustion Institute, Pittsburgh, PA, 1986.

[18] P. Givi, W.-H. Jou, and R. W. Metcalfe, "Flame extinction in a temporally developing mixing layer," in *Proceedings of the Twenty-first Symposium (Int.) on Combustion*, pp. 1251–1261, The Combustion Institute, Pittsburgh, PA, 1986.

[19] P. Givi and W.-H. Jou, "Direct numerical simulations of a two-dimensional reacting, spatially developing mixing layer by a spectral element method," in *Proceedings of the Twenty-second Symposium (Int.) on Combustion*, pp. 635–643, 1988.

[20] F. A. Williams, *Combustion Theory*. The Benjamin/Cummings Publishing Company, Menlo Park, CA, 2nd ed., 1985.

[21] J. P. Drummond, "Two-dimensional numerical simulation of a supersonic, chemically reacting mixing layer," NASA TM 4055, NASA Langely Research Center, 1988.

[22] J. P. Drummond, M. H. Carpenter, and D. W. Riggins, "Mixing and mixing enhancement in supersonic reacting flow fields," in *High Speed Propulsion Systems, Contributions to Thermodynamic Analysis*, AIAA Progress Series, 1990.

[23] D. Gottlieb and E. Turkel, "Dissipative two-four methods for time dependent problems," *Mathematics of Computations*, vol. 30, pp. 703–723, October 1976.

[24] M. H. Carpenter, "A family of dissipative compact two-four schemes," submitted to *Journal of Computational Physics*, 1990.

[25] R. W. MacCormack, *Numerical Solution of the Interaction of a Shock Wave with a Laminar Boundary Layer*, vol. 8 of *Lecture Notes in Physics*, pp. 151–163. Springer-Verlag, 1970.

[26] D. A. Anderson, J. C. Tannehill, and R. H. Pletcher, *Computational Fluid Mechanics and Heat Transfer.* Hemisphere Publishing Corp., 1984.

[27] P. Givi and W.-H. Jou, "Mixing and chemical reactions in a spatially developing mixing layer," *J. Nonequil. Thermodyn.*, vol. 14, pp. 355–372, 1989.

[28] A. Michalke, "On the inviscid instability of the hyperbolic tangent velocity profile," *J. Fluid Mech.*, vol. 19, pp. 543–556, 1964.

[29] C. K. Madnia and P. Givi, "LES and DNS of reacting homogeneous turbulence." To be presented at *International Workshop on Large Eddy Simulations - Where Do We Stand?*, St. Petersburg, FL., December 1990.

[30] C. K. Madnia and P. Givi. Personal communications, October 1990.

[31] P. G. Drazin and W. H. Reid, *Hydrodynamic Stability.* New York, N.Y.: Cambridge University Press, 1981.

[32] T. Hu and P. Givi. Work in progress, 1991.

[33] N. Peters, "Laminar diffusion flamelet models in non-premixed turbulent combustion," *Prog. Energy Comb. Sci.*, vol. 10, pp. 319–339, 1984.

Figures

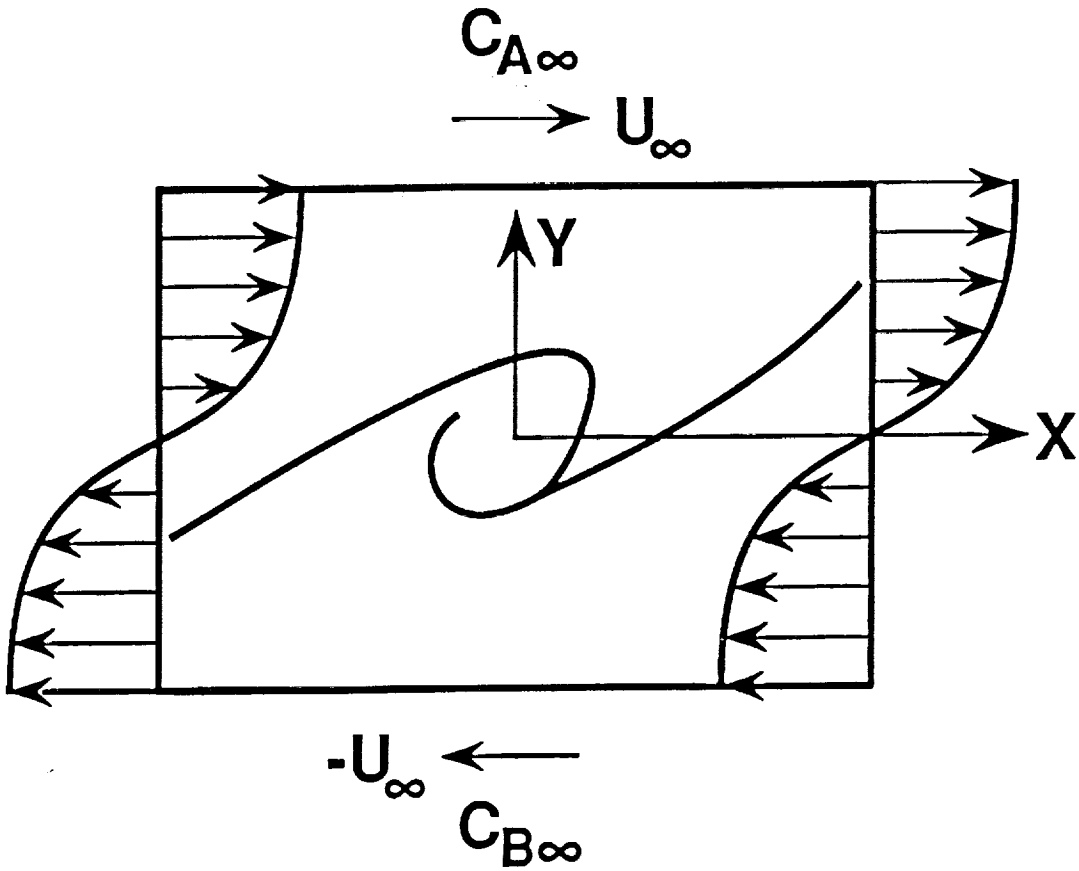

Figure 1: Schematic diagram of a temporally evolving mixing layer.

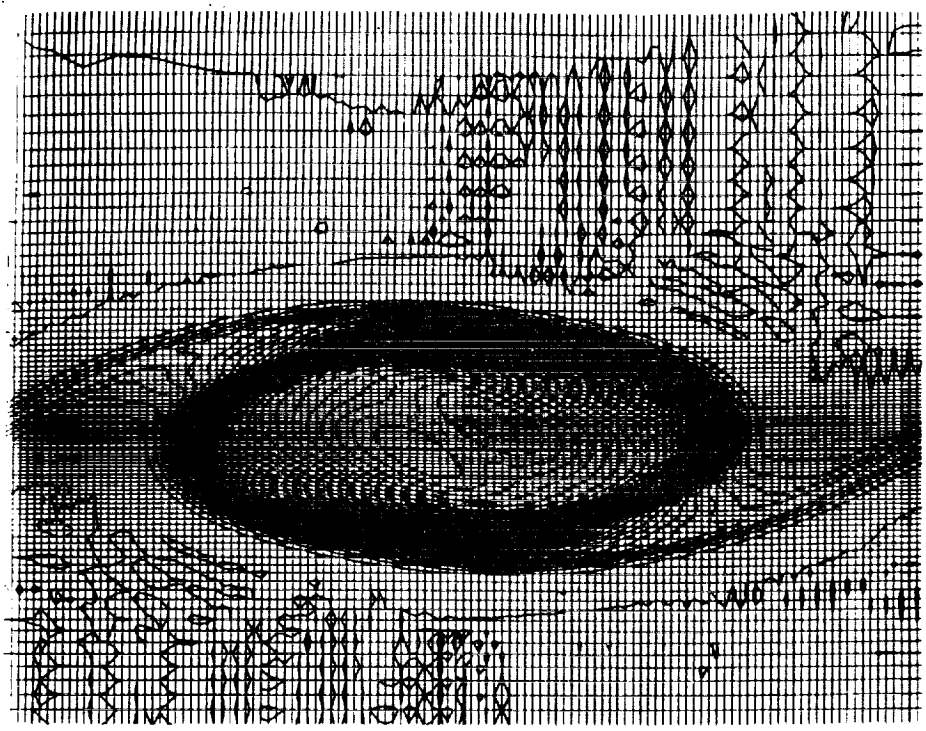

Figure 2: A representative contour plot with the computational grid superimposed.

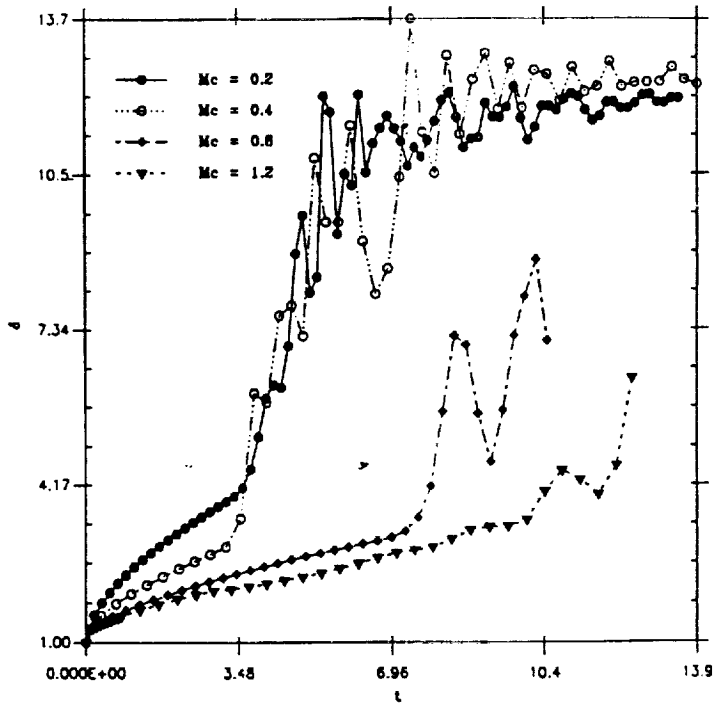

Figure 3: Normalized vorticity thickness versus normalized time for different values of the convective Mach number.

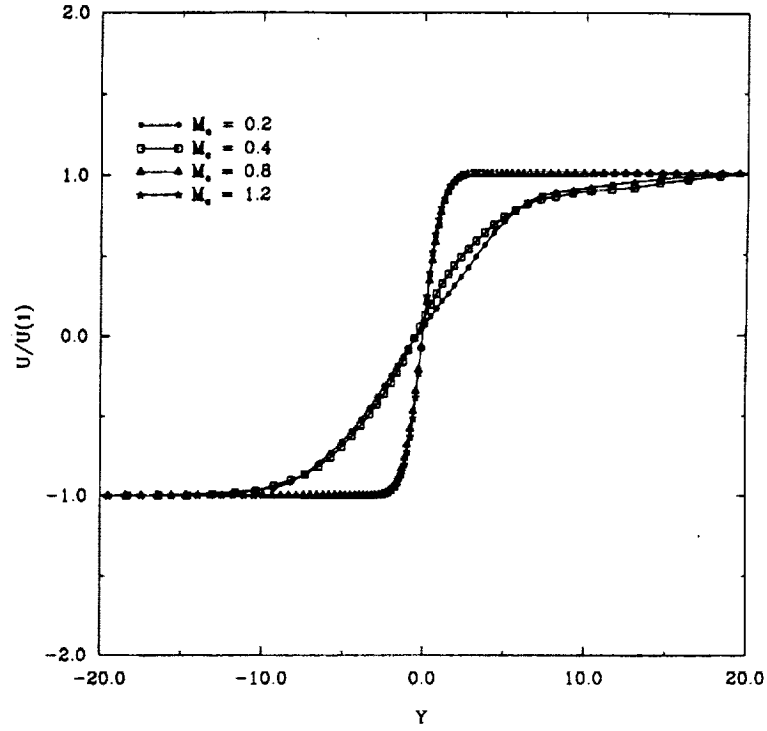

Figure 4: Profiles of normalized mean streamwise velocity for different values of the convective Mach number at time $t^* = 6$.

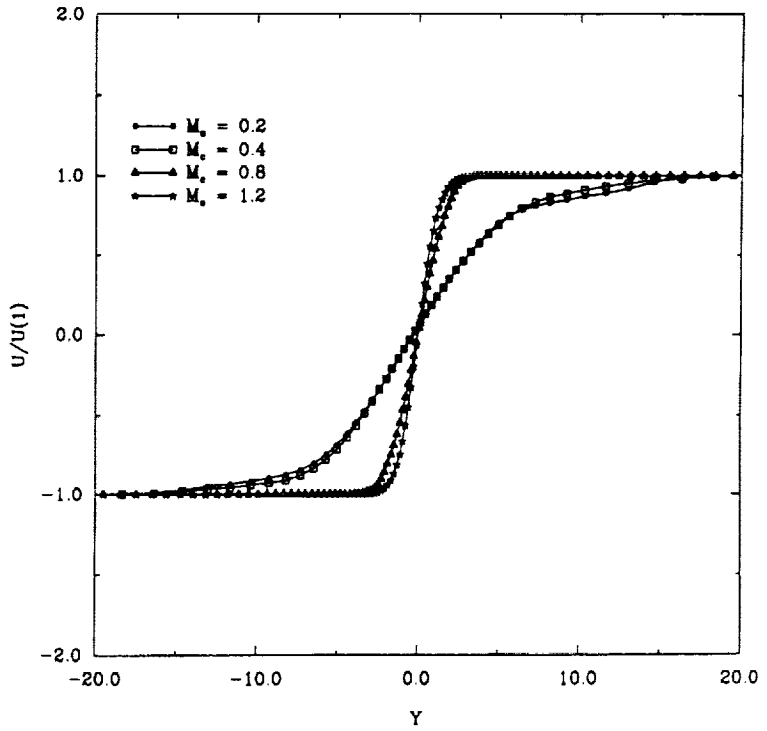

Figure 5: Profiles of normalized mean streamwise velocity for different values of the convective Mach number at time $t^* = 8$.

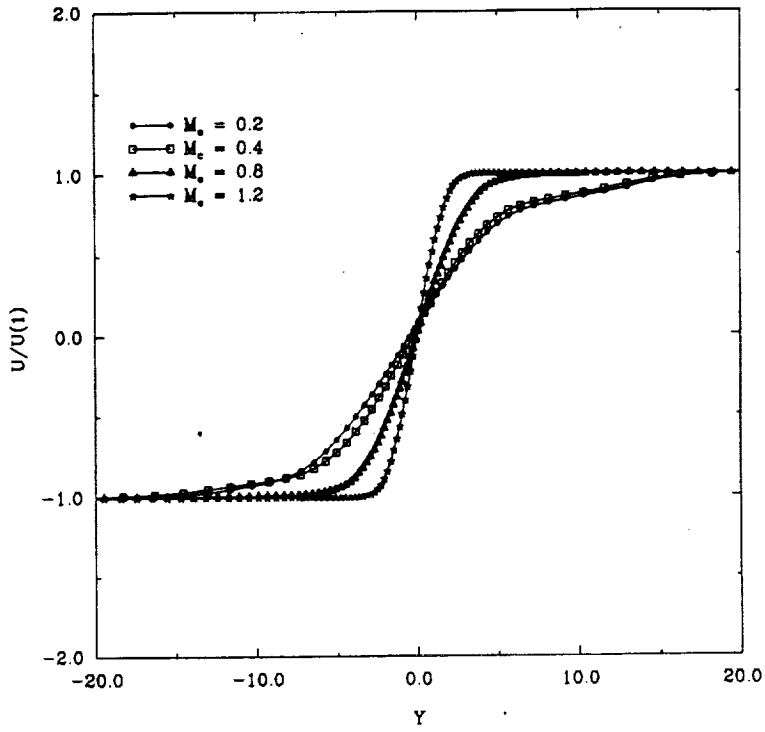

Figure 6: Profiles of normalized mean streamwise velocity for different values of the convective Mach number at time $t^* = 10$.

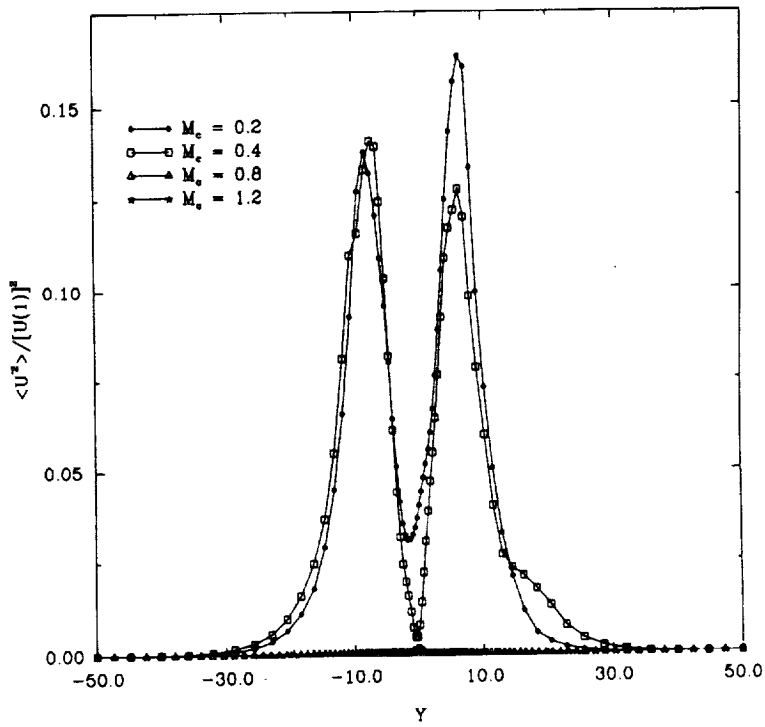

Figure 7: Profiles of normalized mean squared streamwise velocity for different values of the convective Mach number at time $t^* = 6$.

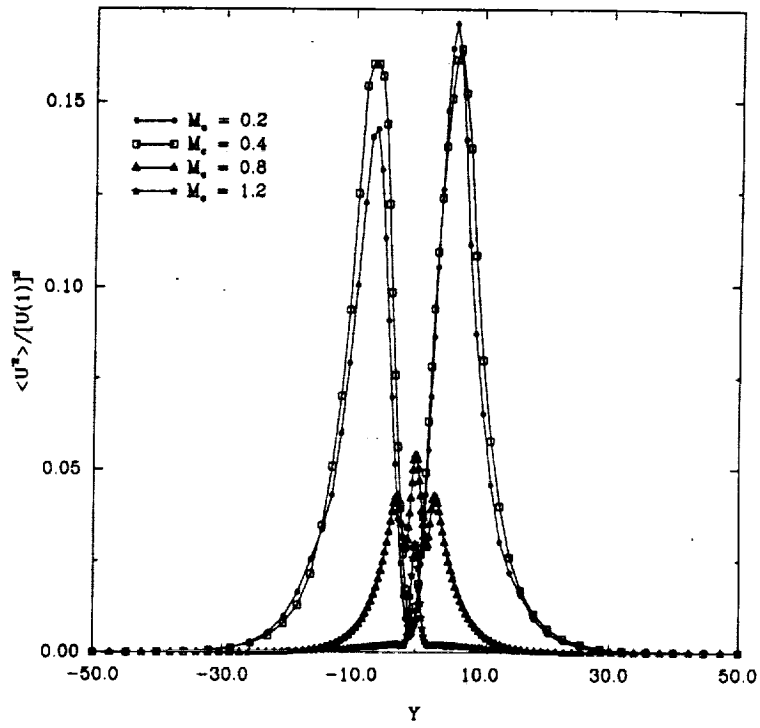

Figure 8: Profiles of normalized mean squared streamwise velocity for different values of the convective Mach number at time $t^* = 8$.

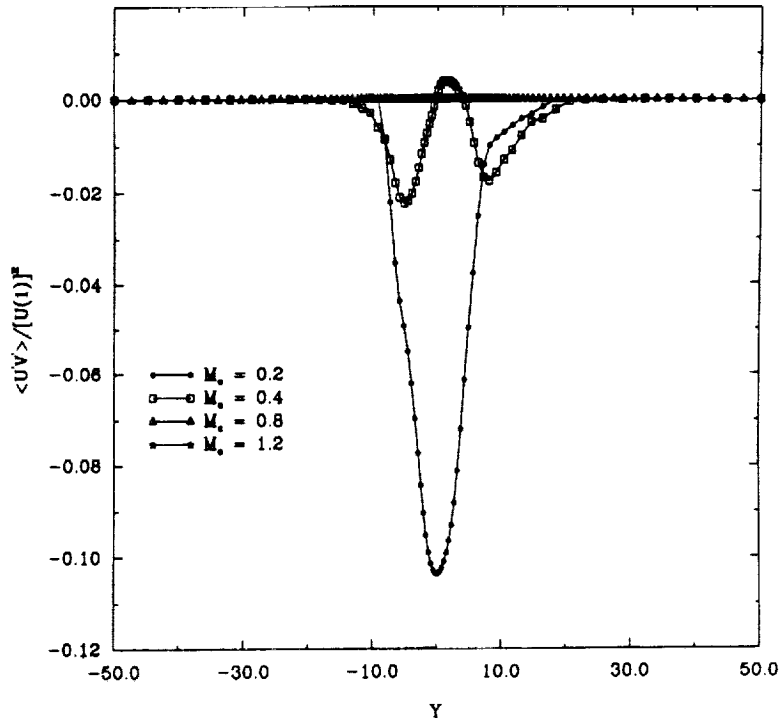

Figure 9: Profiles of normalized Reynolds stress for different values of the convective Mach number at time $t^* = 6$.

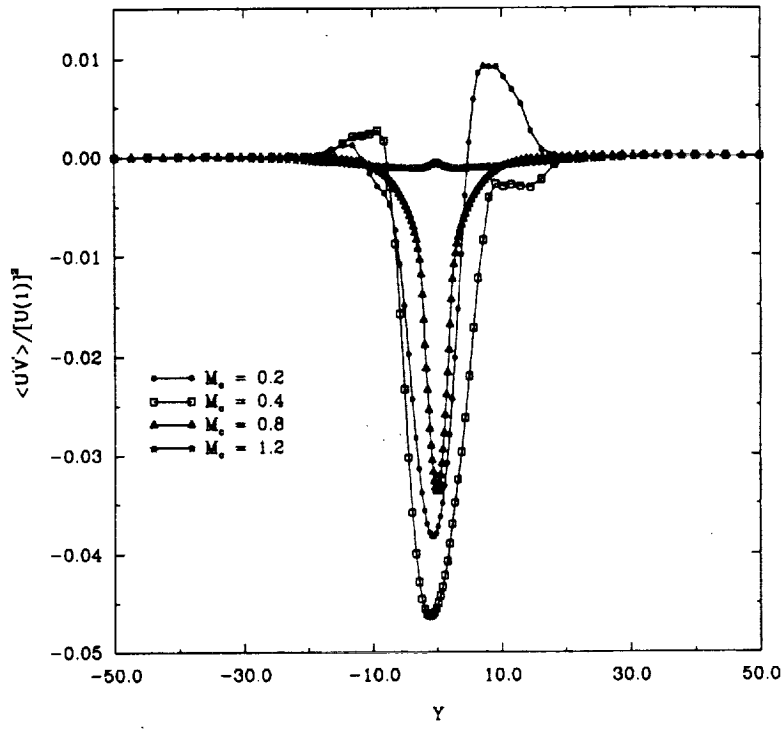

Figure 10: Profiles of normalized Reynolds stress for different values of the convective Mach number at time $t^* = 8$.

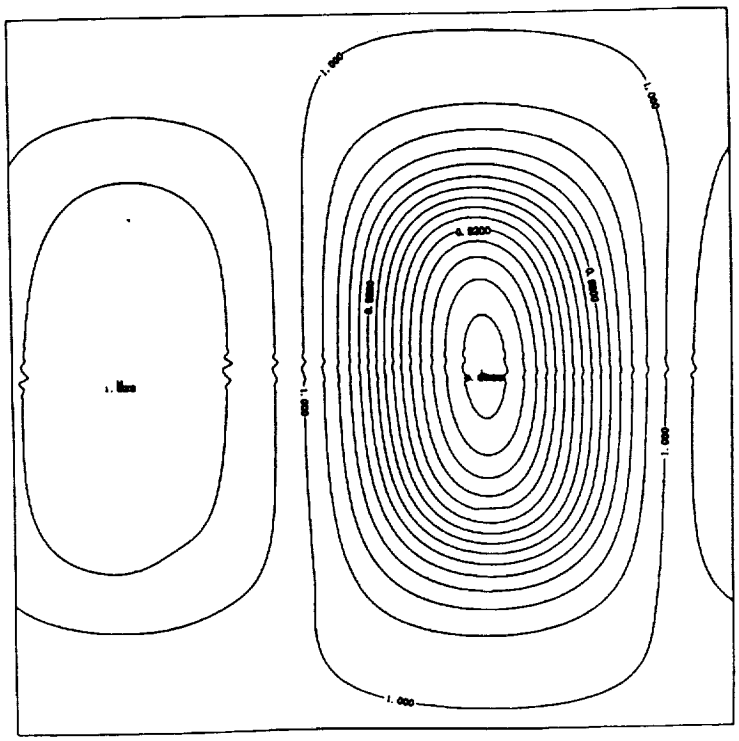

Figure 11: Plot of pressure contours at time $t^* = 8$, $M_c = 0.2$

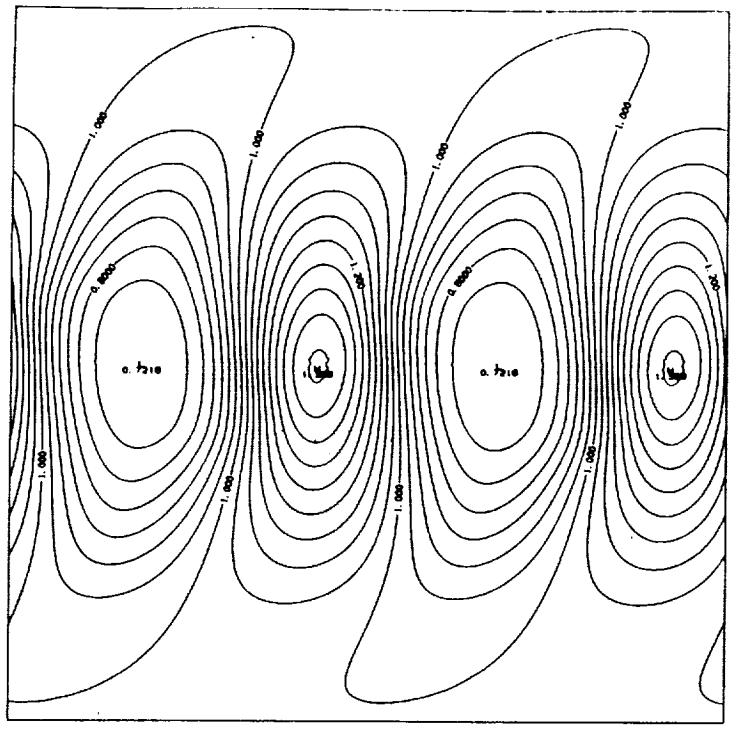

Figure 12: Plot of pressure contours at time $t^* = 8$, $M_c = 0.8$

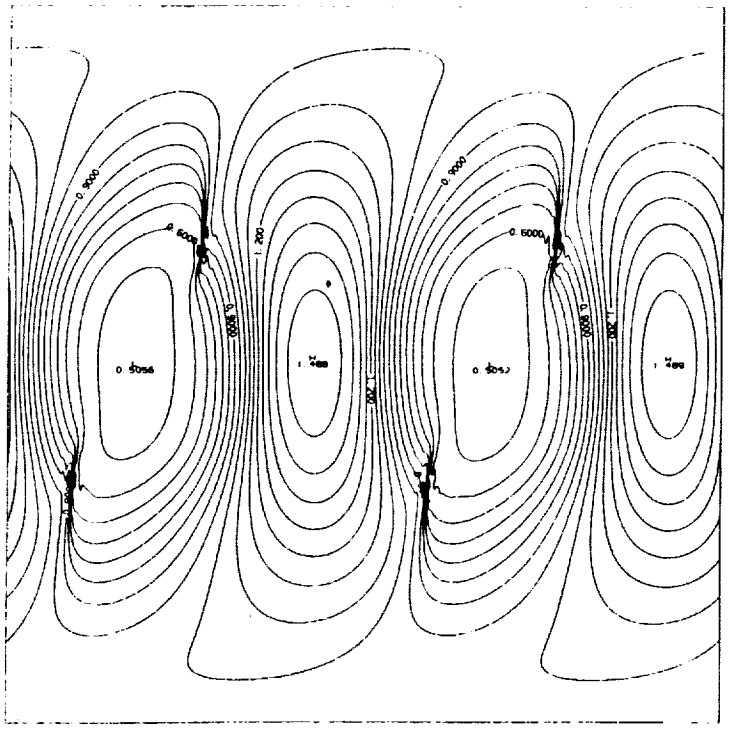

Figure 13: Plot of pressure contours at time $t^* = 8.5$, $M_c = 0.8$

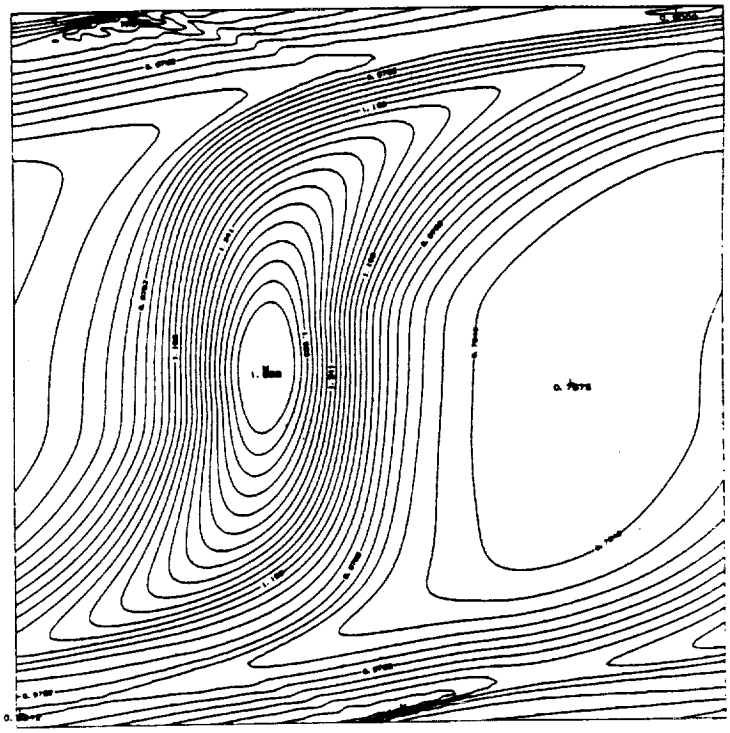

Figure 14: Plot of pressure contours at time $t^* = 10$, $M_c = 1.2$

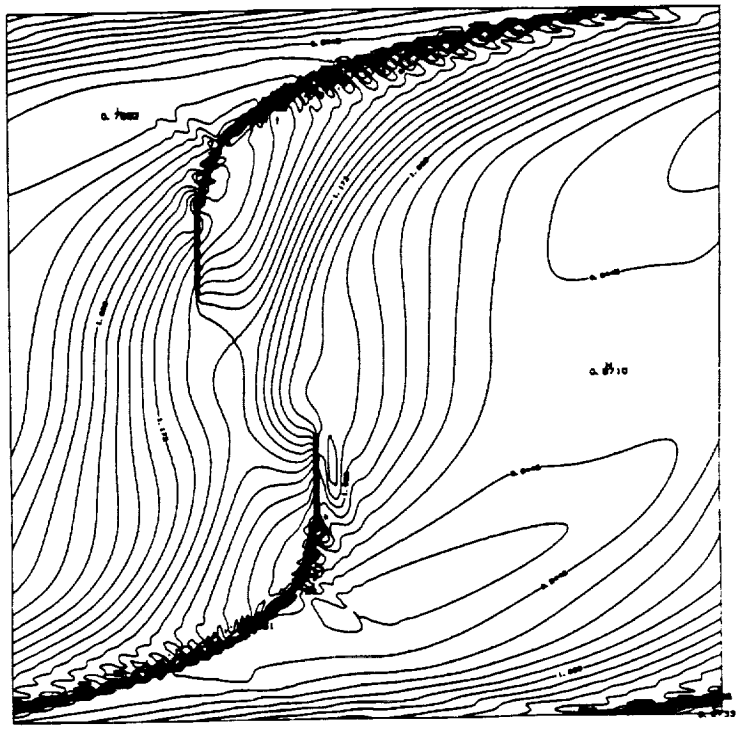

Figure 15: Plot of pressure contours at time $t^* = 10.85$, $M_c = 1.2$

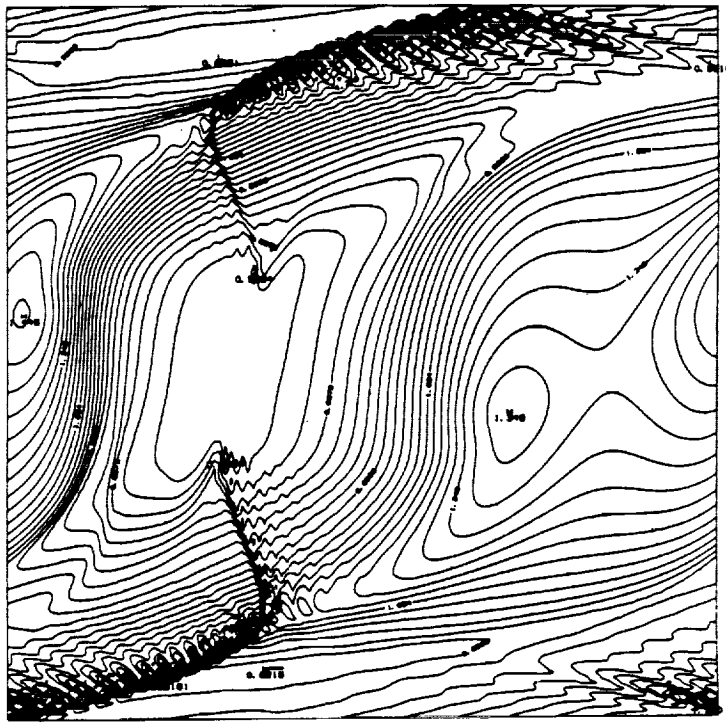

Figure 16: Plot of pressure contours at time $t^* = 11.66$, $M_c = 1.2$

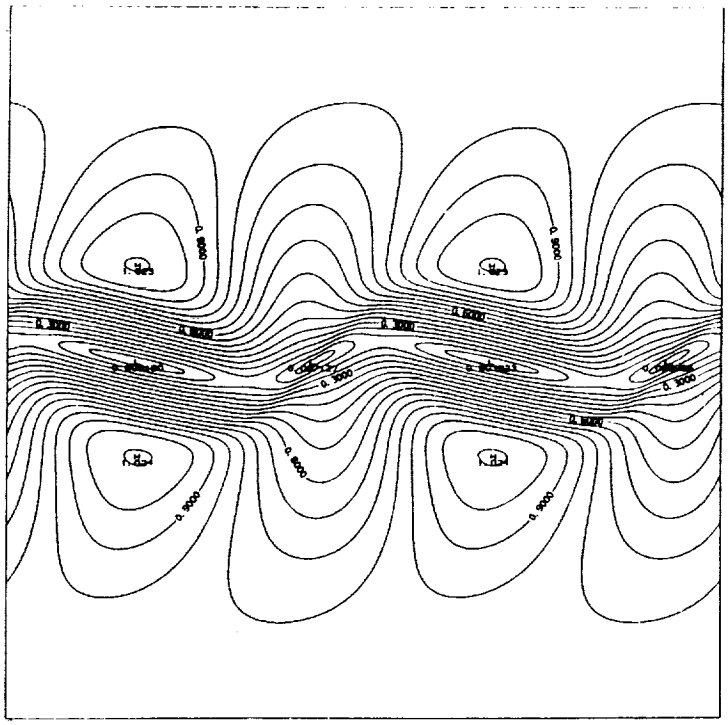

Figure 17: Plot of Mach number contours at time $t^* = 8$, $M_c = 0.8$

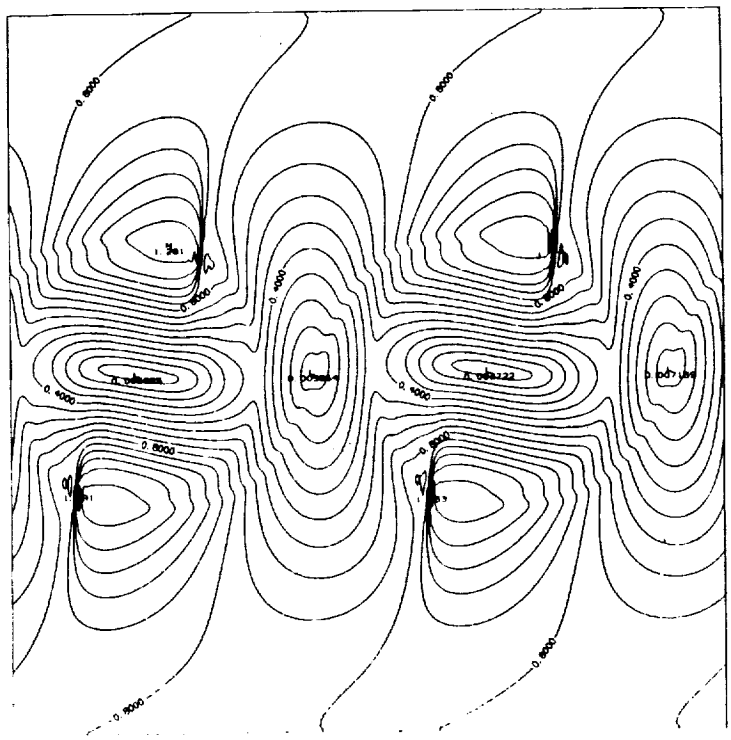

Figure 18: Plot of Mach number contours at time $t^* = 8.5$, $M_c = 0.8$

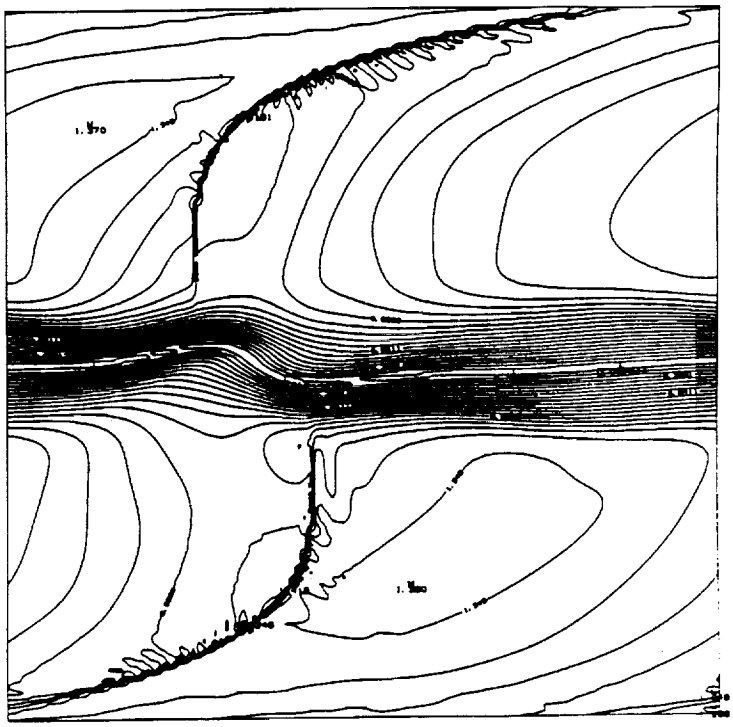

Figure 19: Plot of Mach number contours at time $t^* = 10.85$, $M_c = 1.2$.

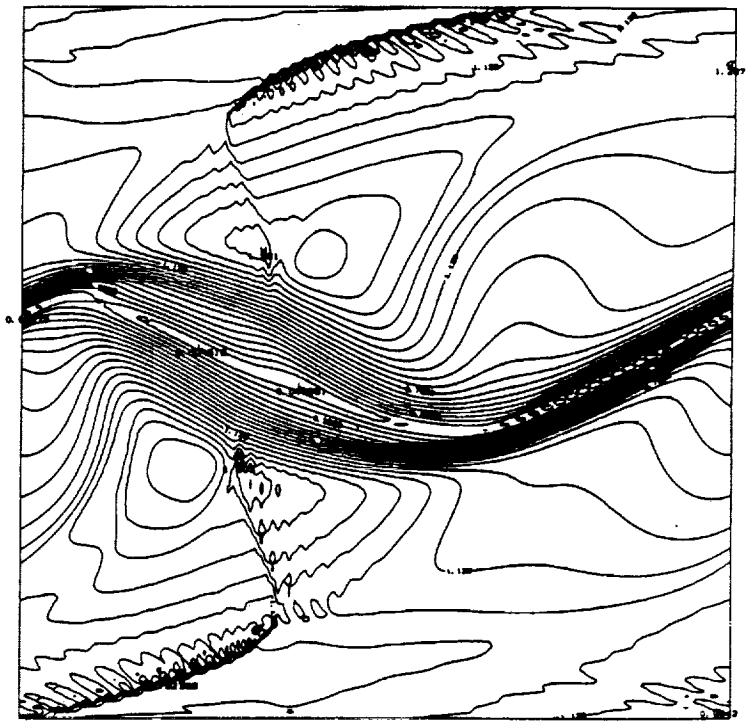

Figure 20: Plot of Mach number contours at time $t^* = 11.66$, $M_c = 1.2$.

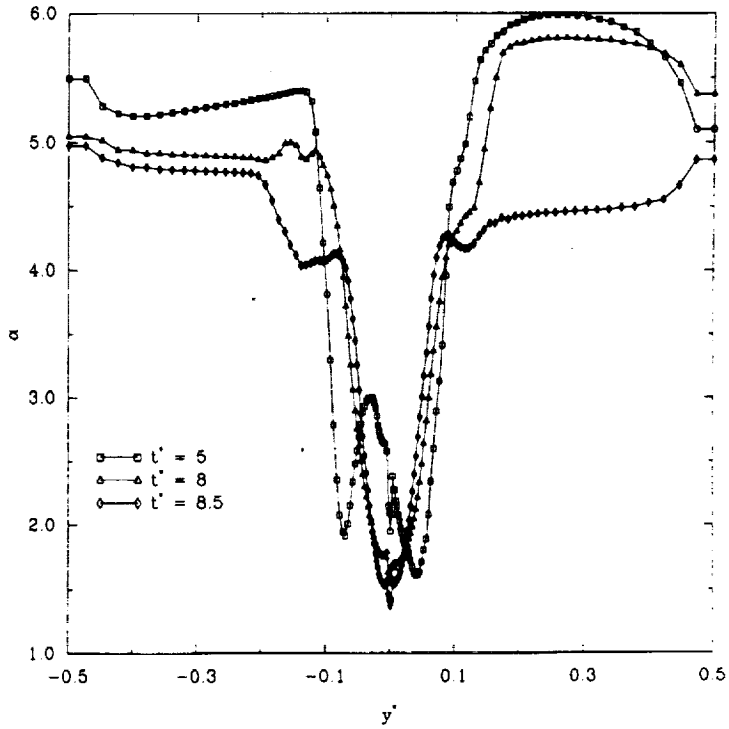

Figure 21: Profile of ratio of the rms Mach number to the normalized rms density for $M_c = 0.2$

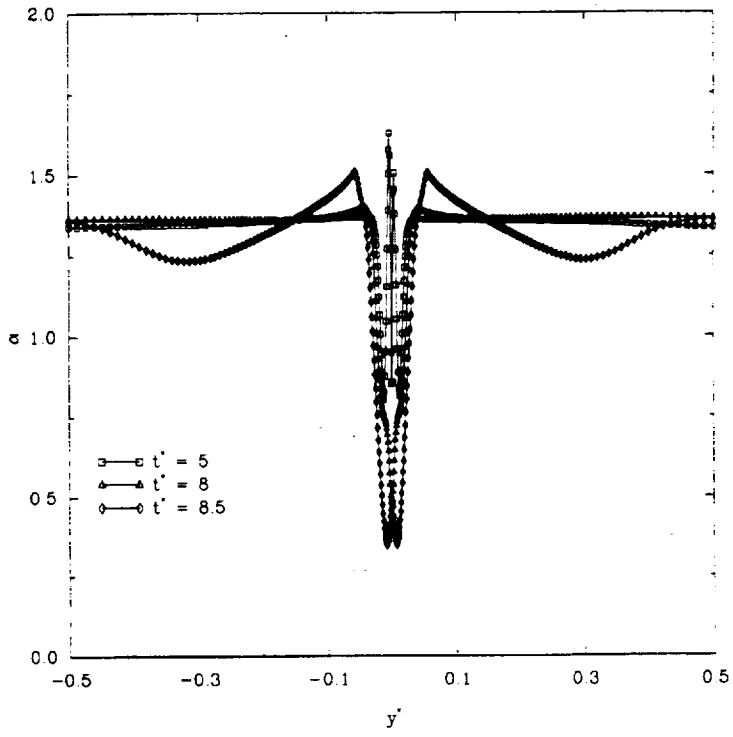

Figure 22: Profile of ratio of the rms Mach number to the normalized rms density for $M_c = 0.8$

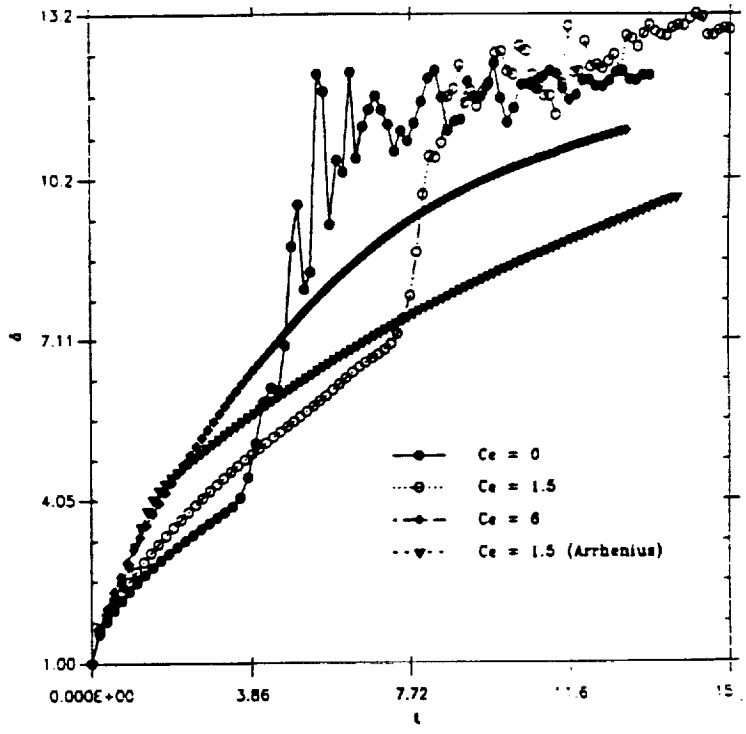

Figure 23: Normalized vorticity thickness versus normalized time for different values of the heat release parameter.

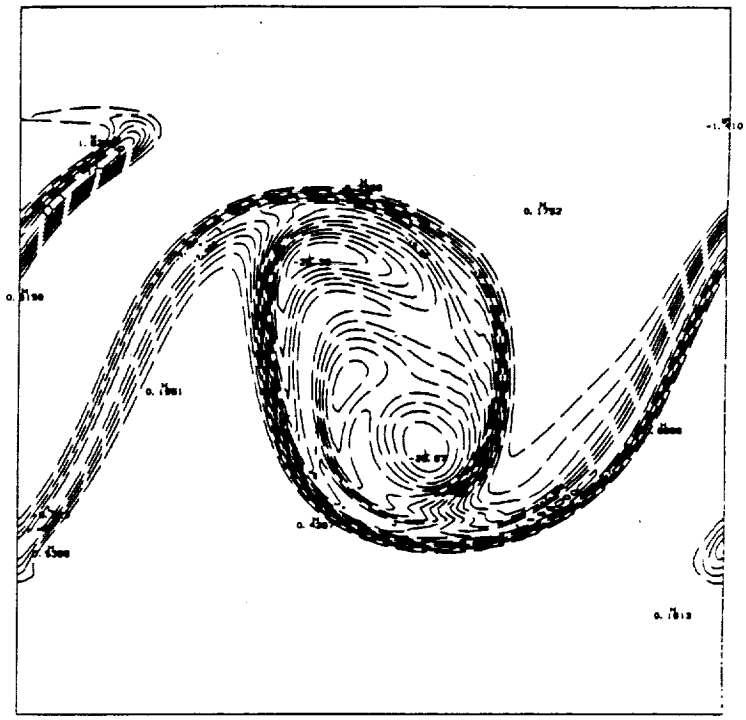

Figure 24: Plot of vorticity contours at time $t^* = 6$, $C_e = 0$

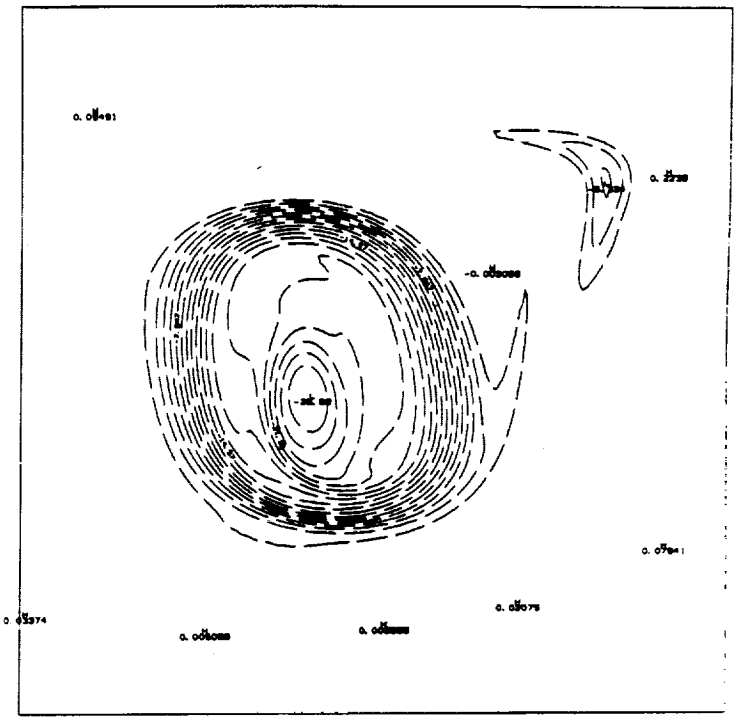

Figure 25: Plot of vorticity contours at time $t^* = 8$, $C_e = 0$

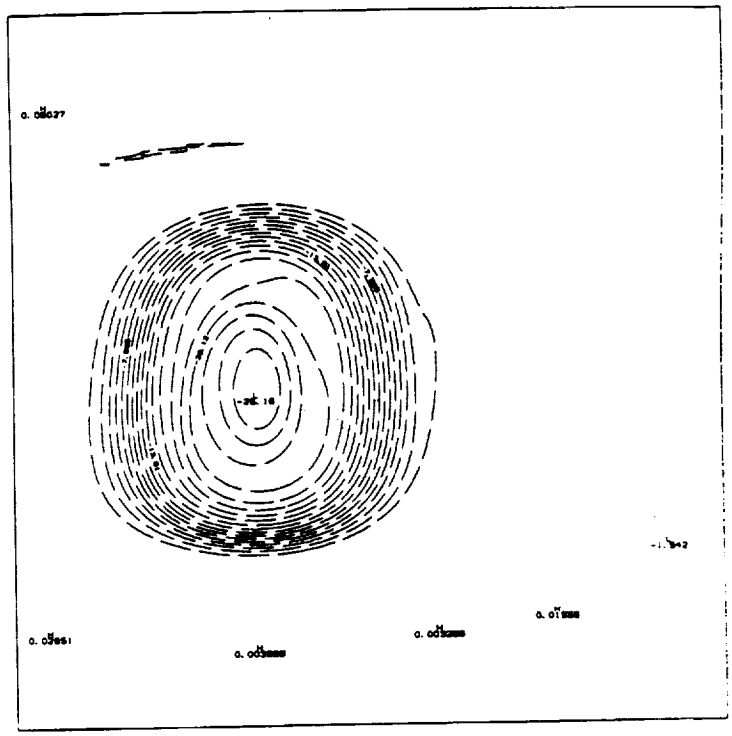

Figure 26: Plot of vorticity contours at time $t^* = 10$, $C_e = 0$

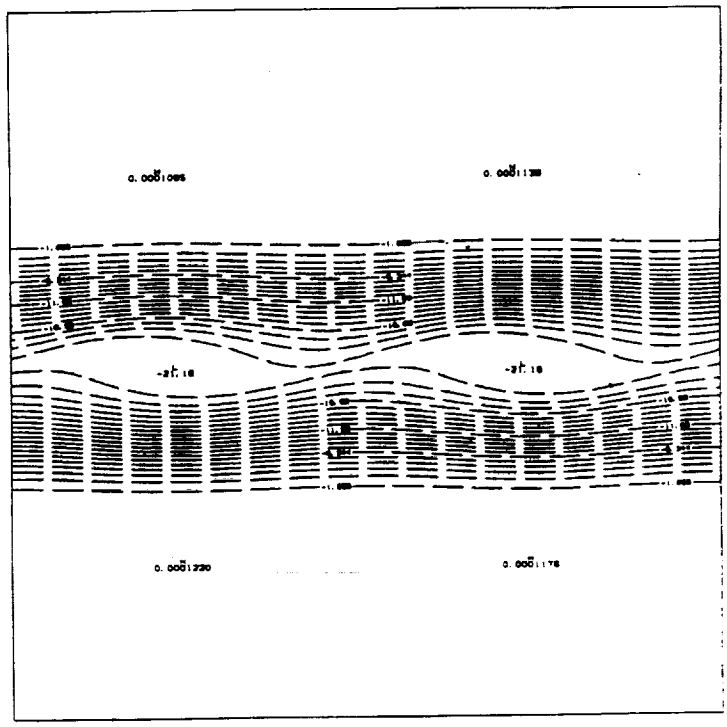

Figure 27: Plot of vorticity contours at time $t^* = 6$, $C_e = 1.5$

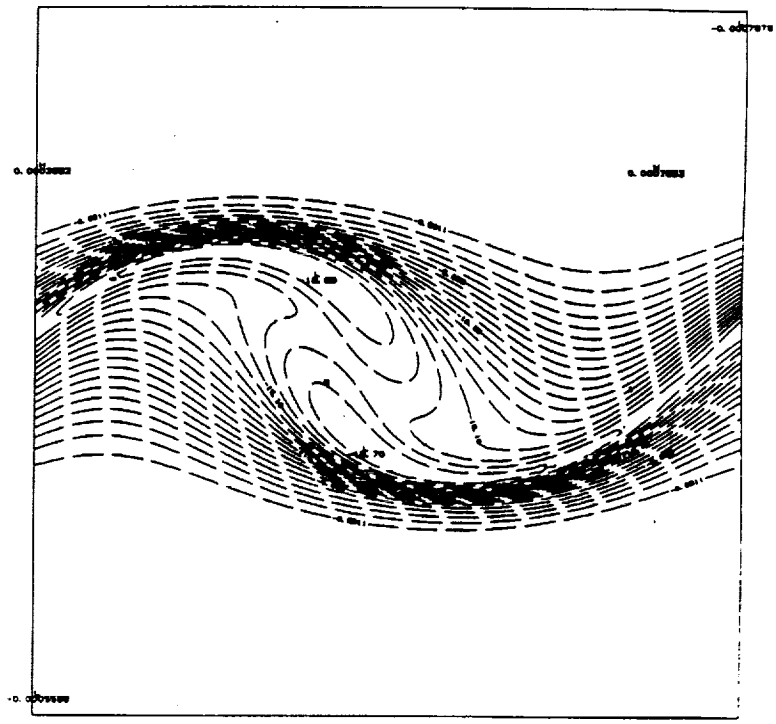

Figure 28: Plot of vorticity contours at time $t^* = 8$, $C_e = 1.5$

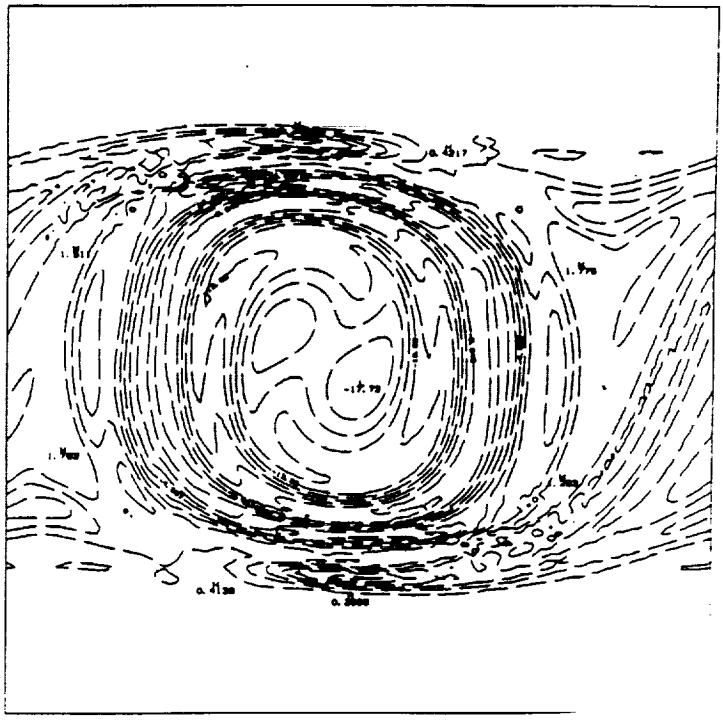

Figure 29: Plot of vorticity contours at time $t^* = 10$, $C_e = 1.5$

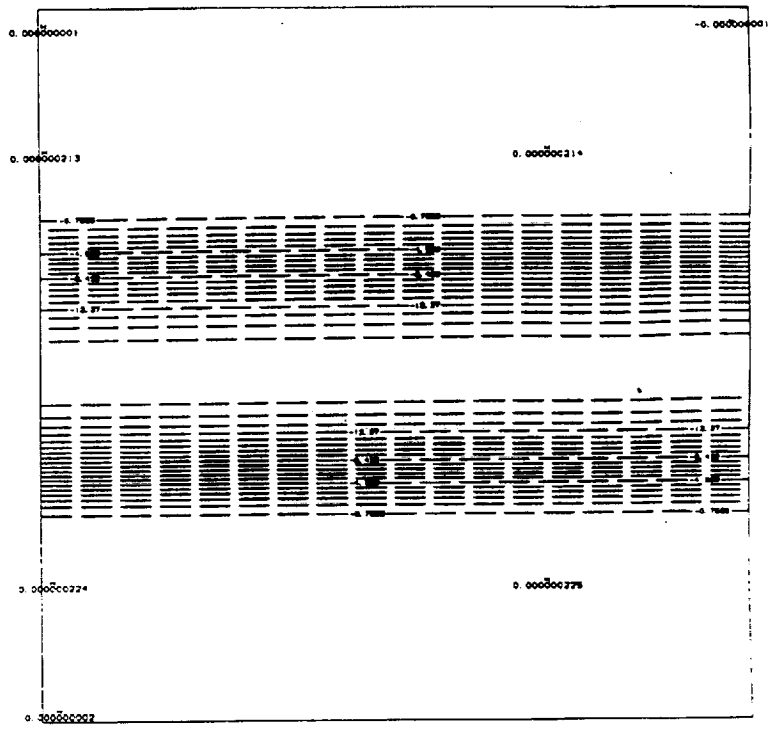

Figure 30: Plot of vorticity contours at time $t^* = 6$, $C_e = 6$

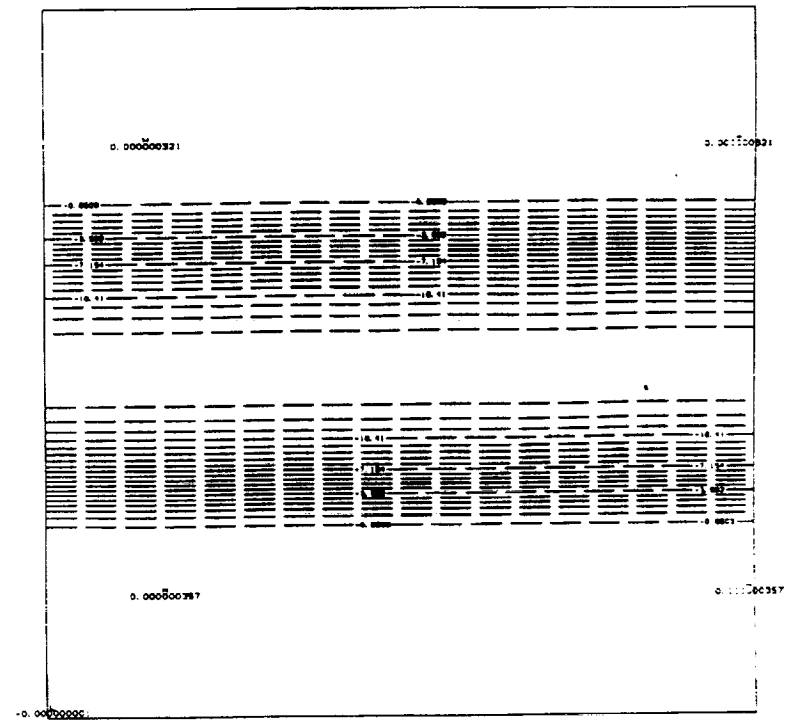

Figure 31: Plot of vorticity contours at time $t^* = 8$, $C_e = 6$

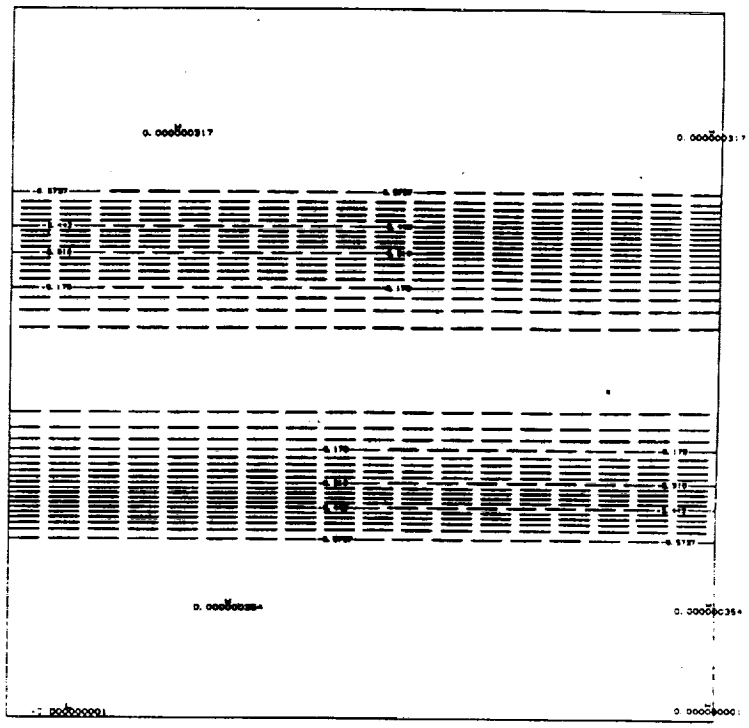

Figure 32: Plot of vorticity contours at time $t^* = 10$, $C_e = 6$

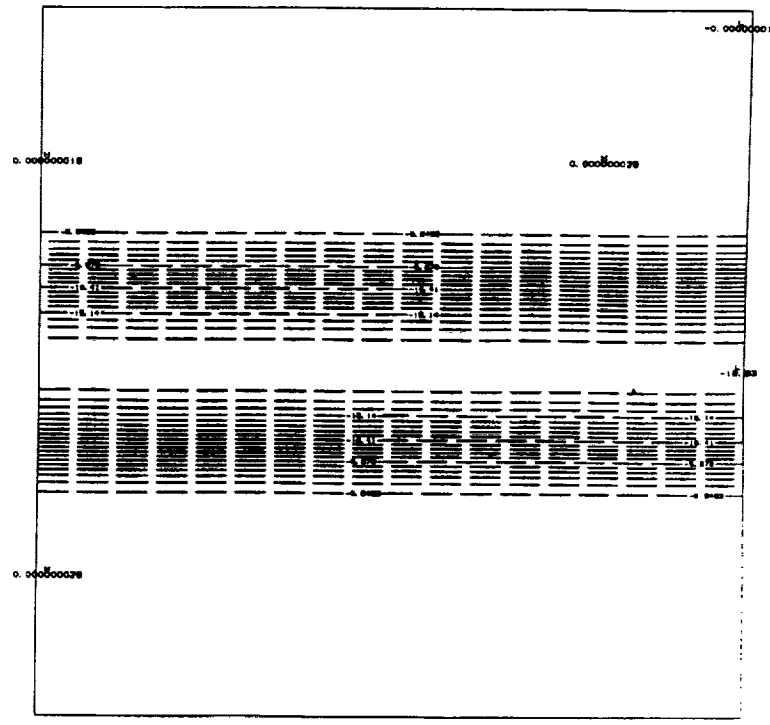

Figure 33: Plot of vorticity contours at time $t^* = 8$, $C_e = 1.5$, and Arrhenius kinetics model.

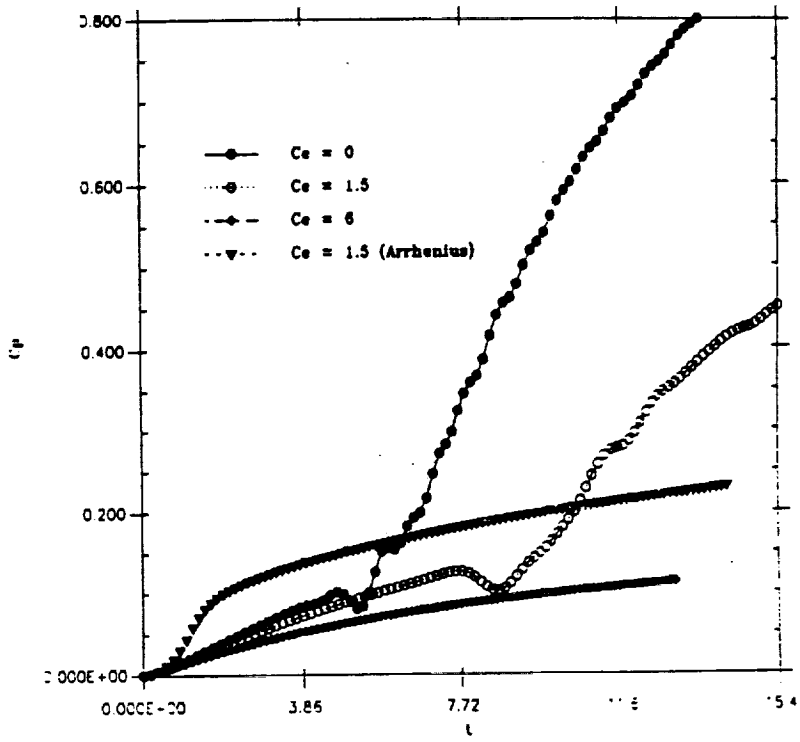

Figure 34: Normalized product thickness versus normalized time for various values of the heat release parameter.

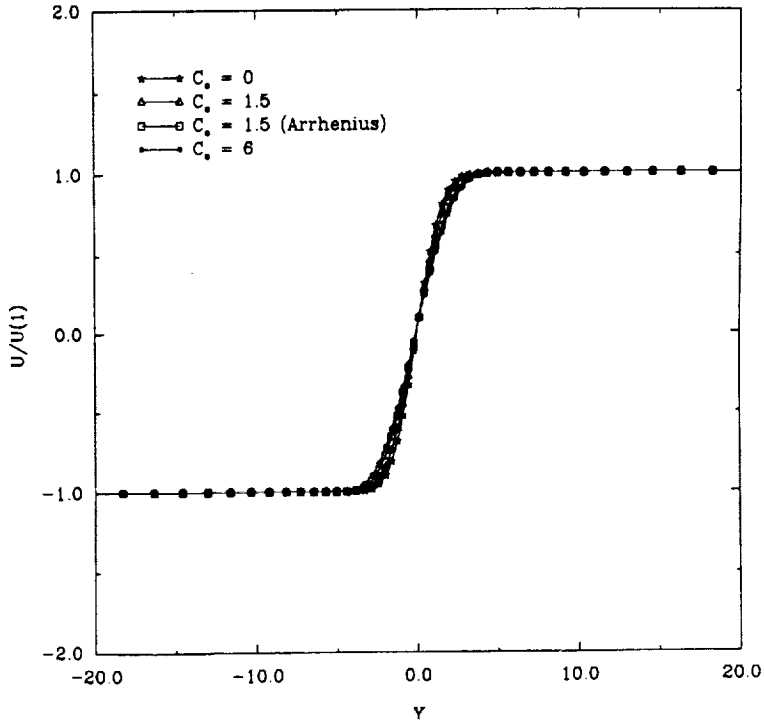

Figure 35: Profiles of normalized mean streamwise velocity for different values of the heat release parameter at time $t^* = 3$.

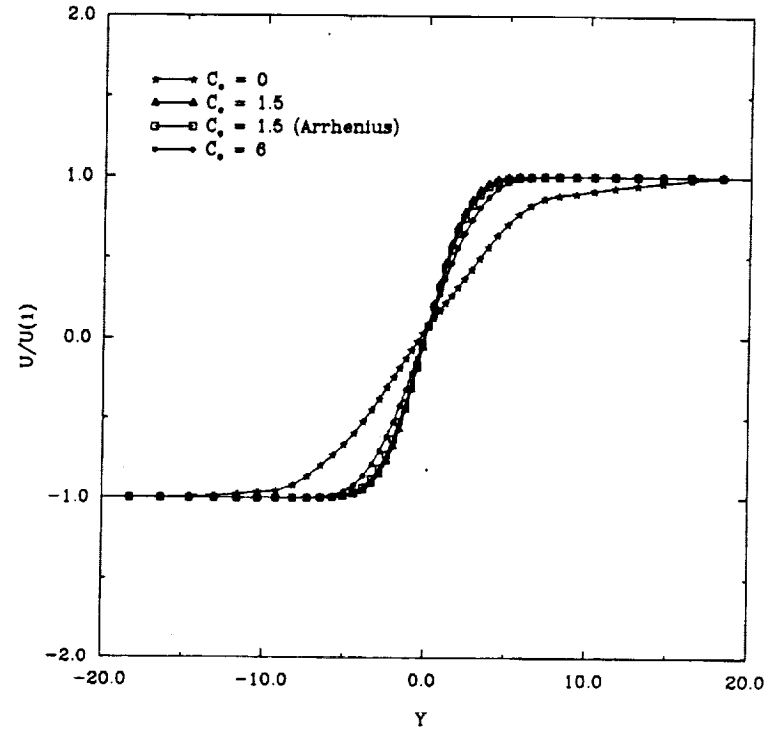

Figure 36: Profiles of normalized mean streamwise velocity for different values of the heat release parameter at time $t^* = 6$.

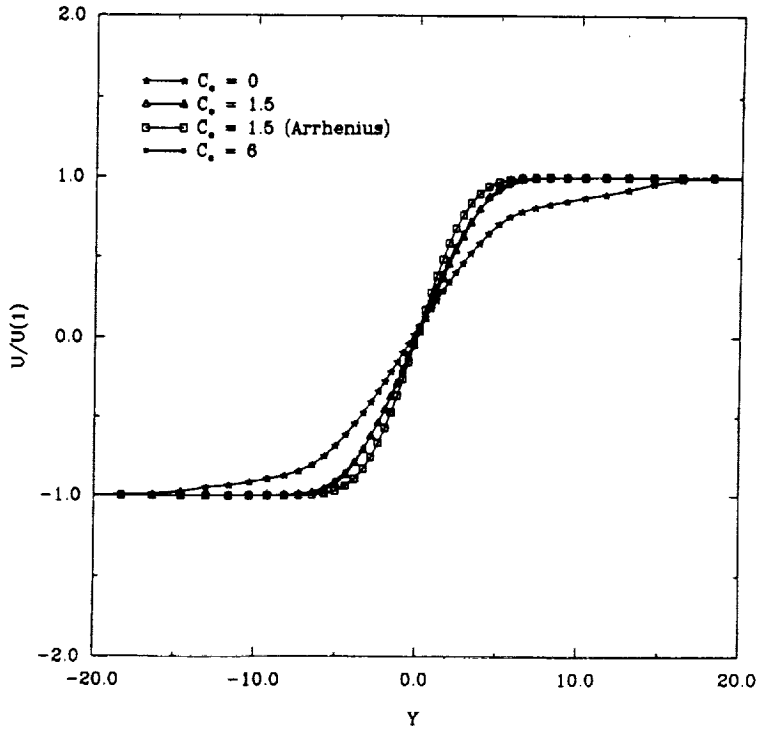

Figure 37: Profiles of normalized mean streamwise velocity for different values of the heat release parameter at time $t^* = 8$.

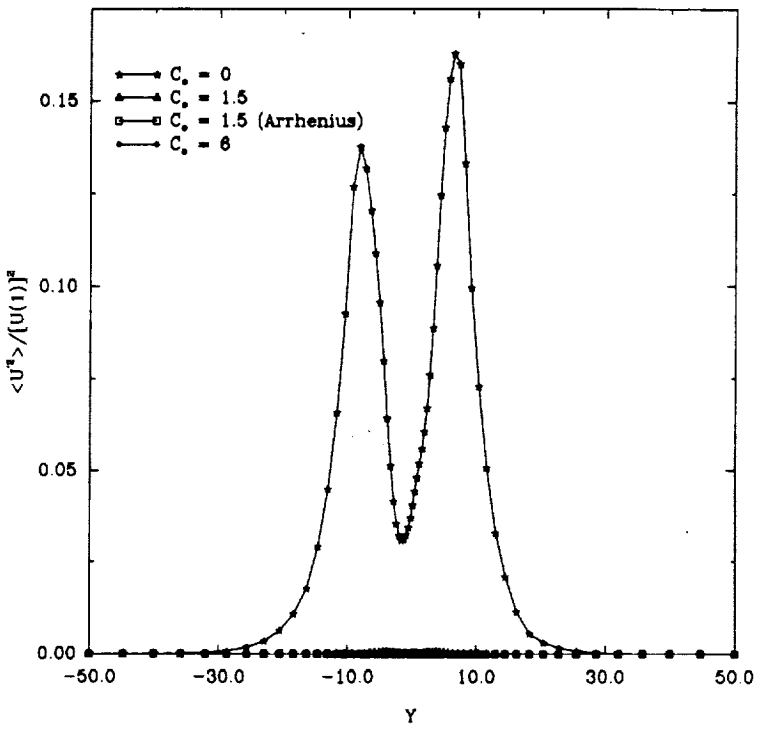

Figure 38: Profiles of normalized mean squared streamwise velocity for different values of the heat release parameter at time $t^* = 6$.

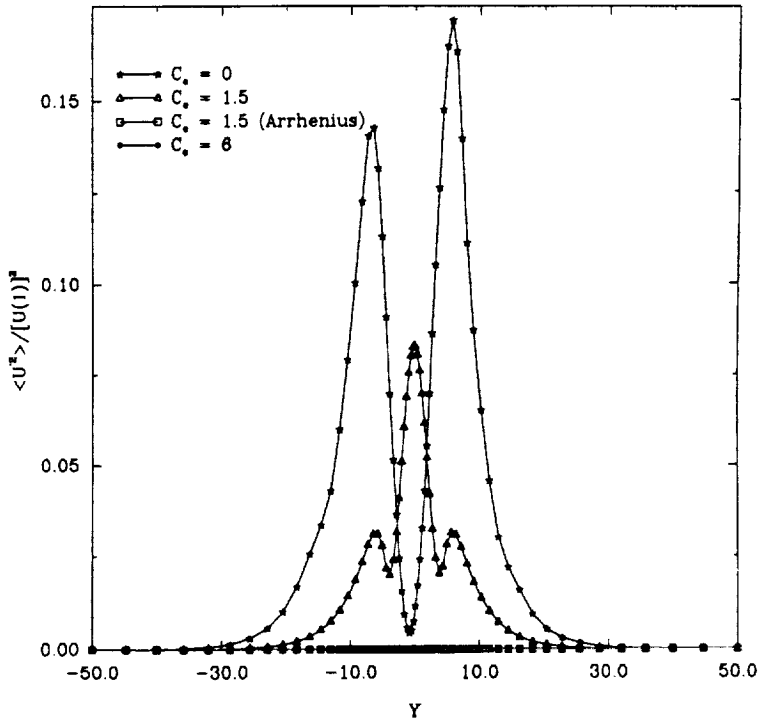

Figure 39: Profiles of normalized mean squared streamwise velocity for different values of the heat release parameter at time $t^* = 8$.

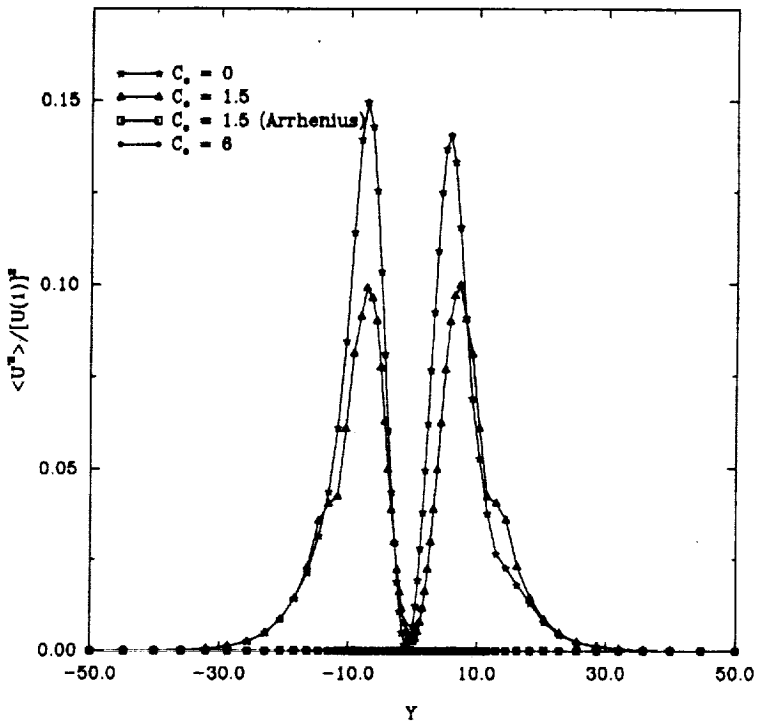

Figure 40: Profiles of normalized mean squared streamwise velocity for different values of the heat release parameter at time $t^* = 10$.

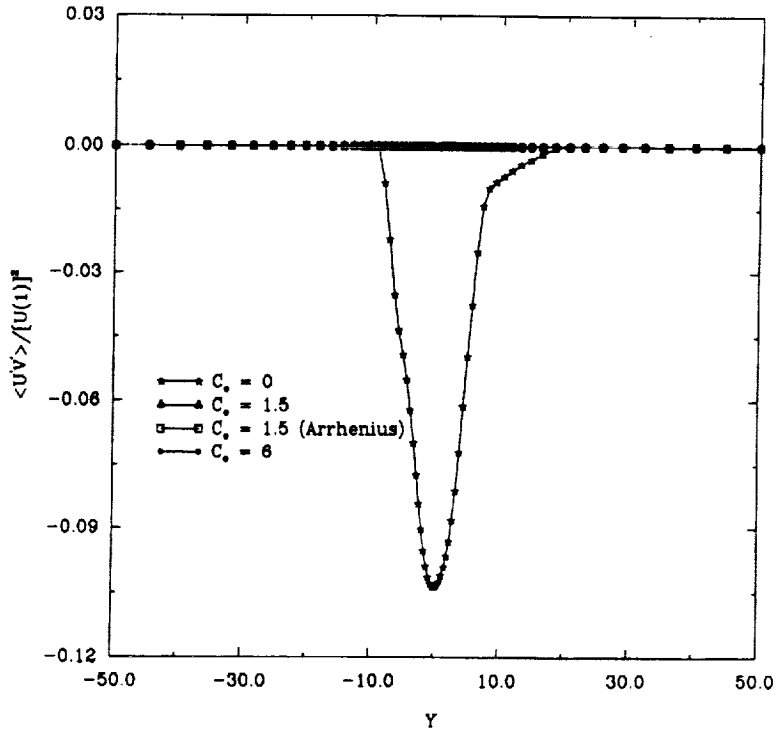

Figure 41: Profiles of normalized Reynolds stress for different values of the heat release parameter at time $t^* = 6$.

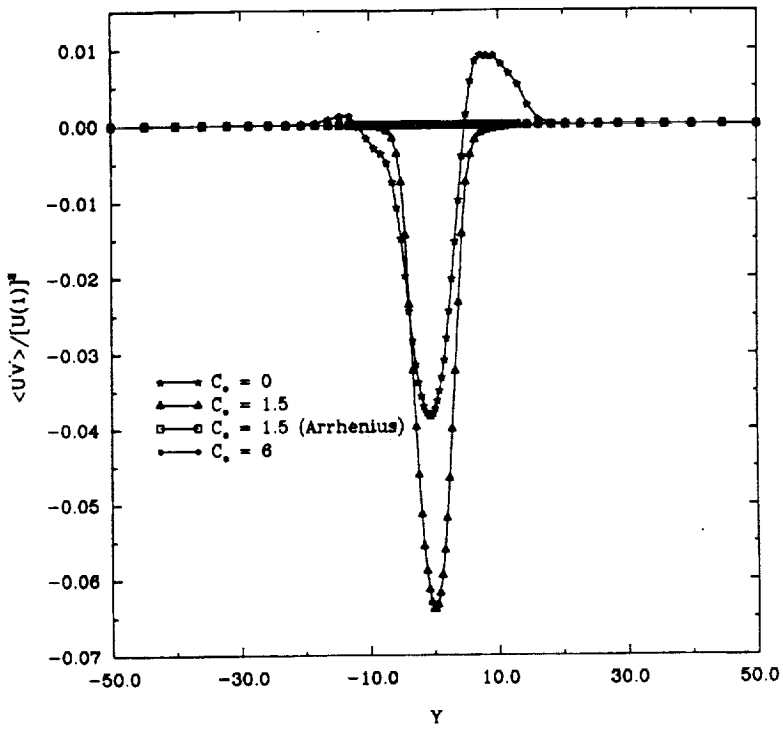

Figure 42: Profiles of normalized Reynolds stress for different values of the heat release parameter at time $t^* = 8$.

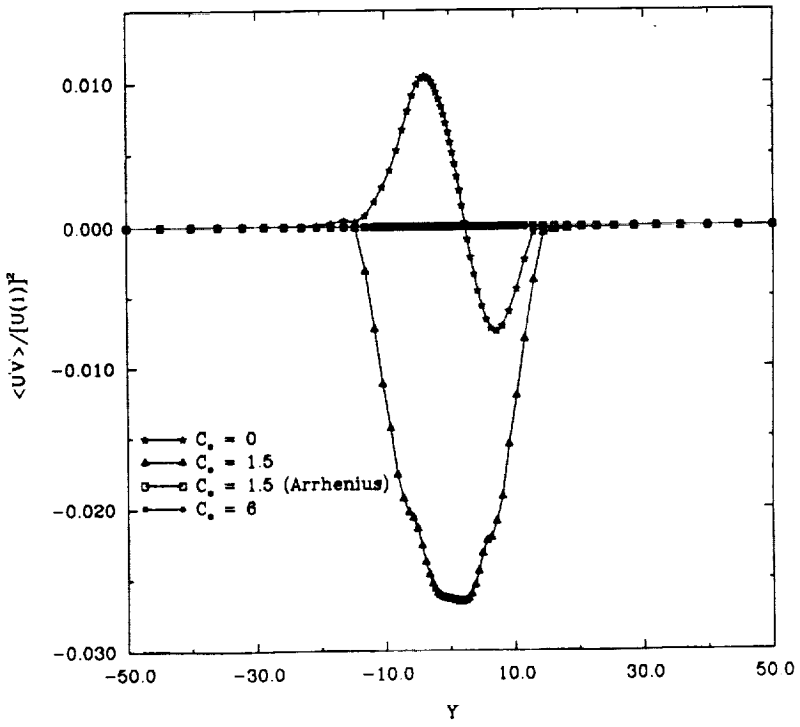

Figure 43: Profiles of normalized Reynolds stress for different values of the heat release parameter at time $t^* = 10$.

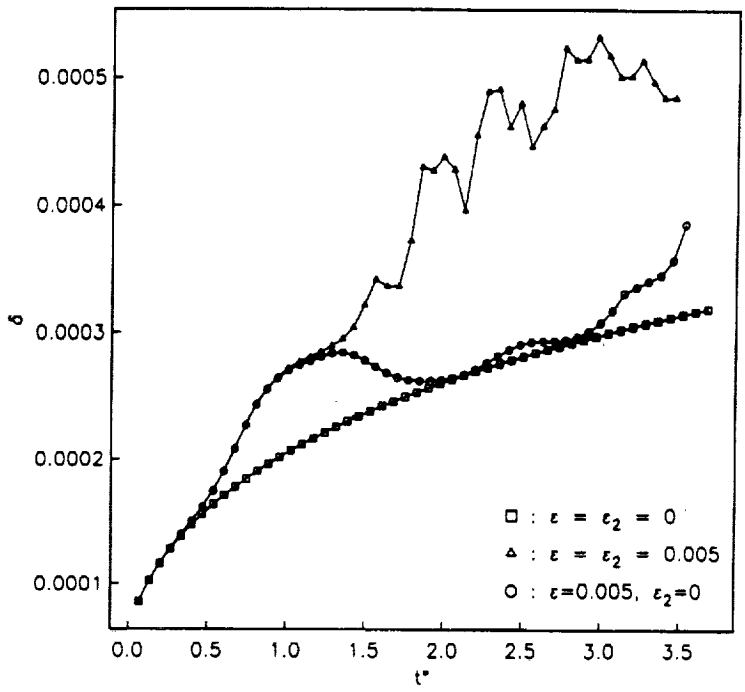

Figure 44: Normalized vorticity thickness versus normalized time for different forcing parameters.

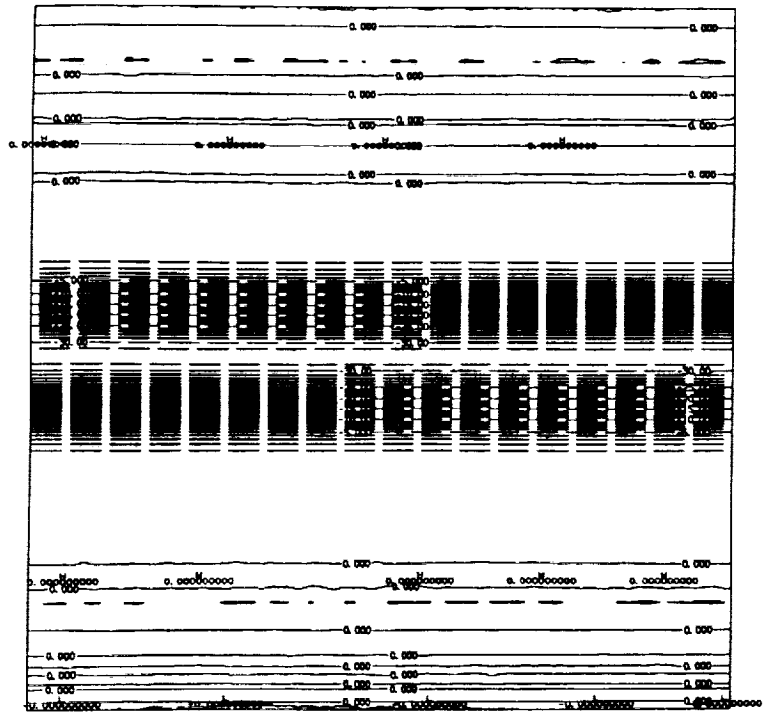

Figure 45: Plot of vorticity contours for $\epsilon_1 = \epsilon_2 = 0$ at time $t^* = 1$.

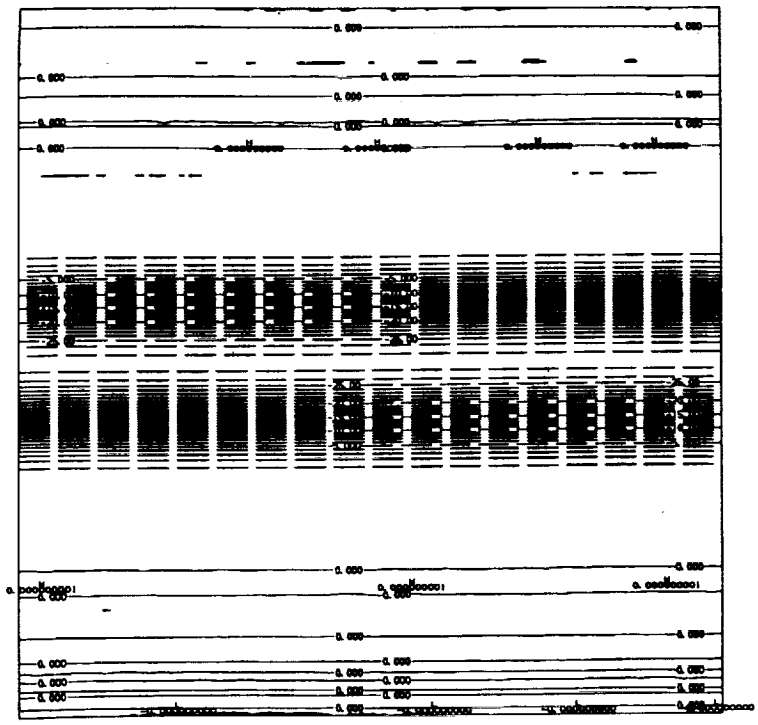

Figure 46: Plot of vorticity contours for $\epsilon_1 = \epsilon_2 = 0$ at time $t^* = 1.5$.

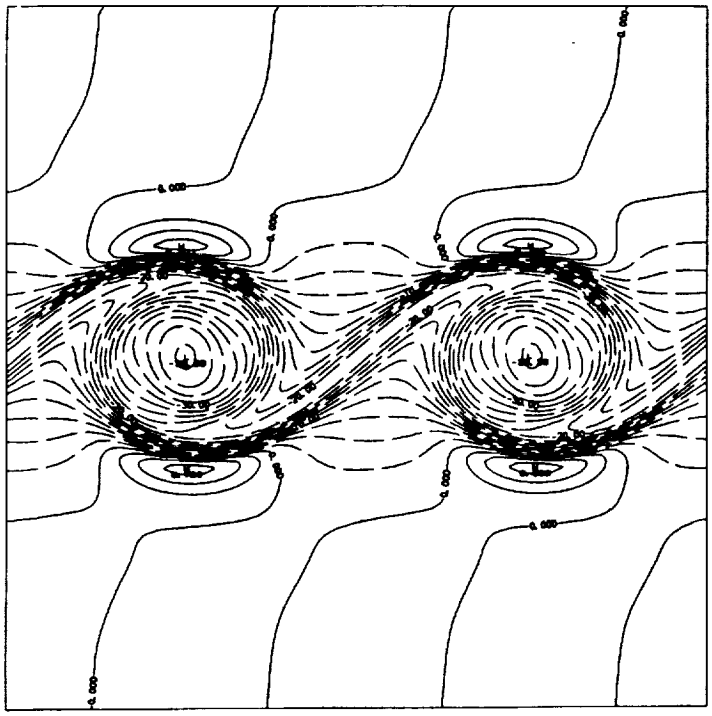

Figure 47: Plot of vorticity contours for $\epsilon_1 = 0.005$, $\epsilon_2 = 0$ at time $t^* = 1$.

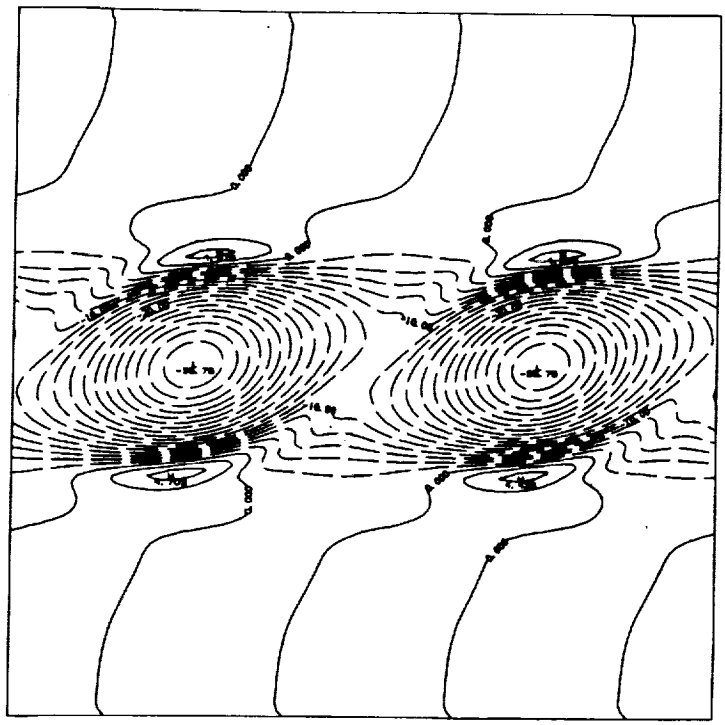

Figure 48: Plot of vorticity contours for $\epsilon_1 = 0.005$, $\epsilon_2 = 0$ at time $t^* = 1.5$.

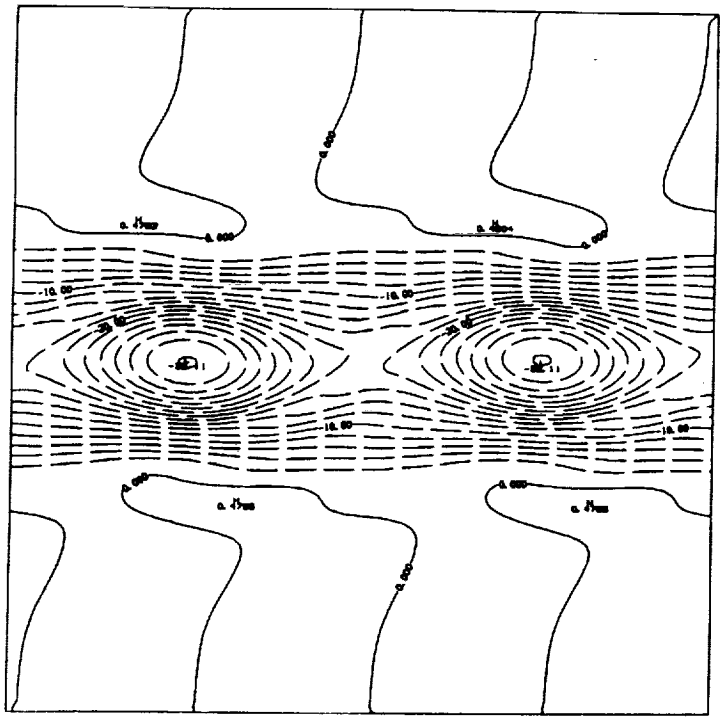

Figure 49: Plot of vorticity contours for $\epsilon_1 = 0.005$, $\epsilon_2 = 0$ at time $t^* = 2.1$.

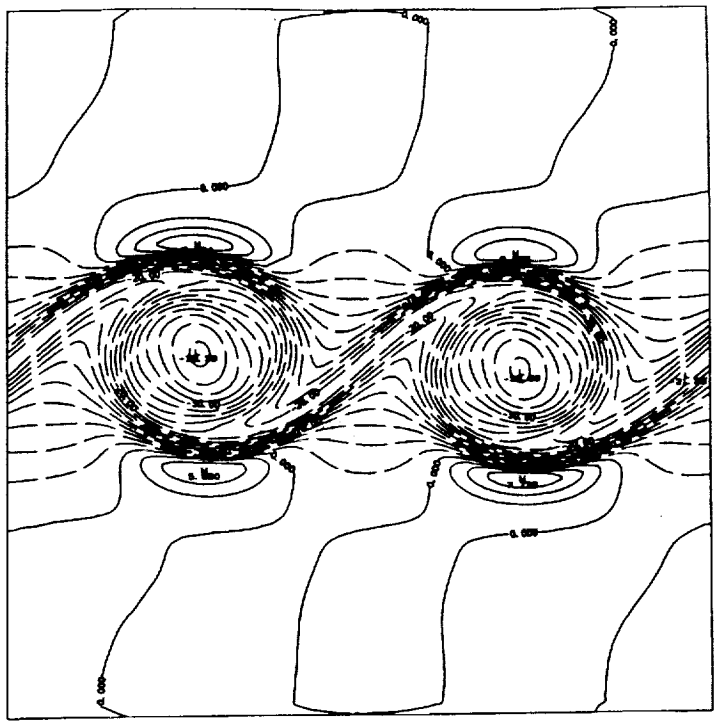

Figure 50: Plot of vorticity contours for $\epsilon_1 = \epsilon_2 = 0.005$ at time $t^* = 1$.

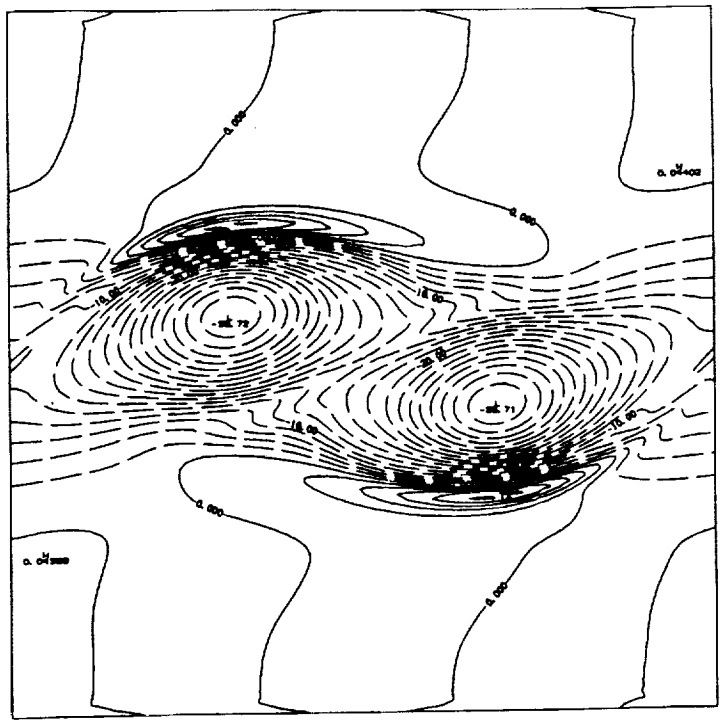

Figure 51: Plot of vorticity contours for $\epsilon_1 = \epsilon_2 = 0.005$ at time $t^* = 1.5$.

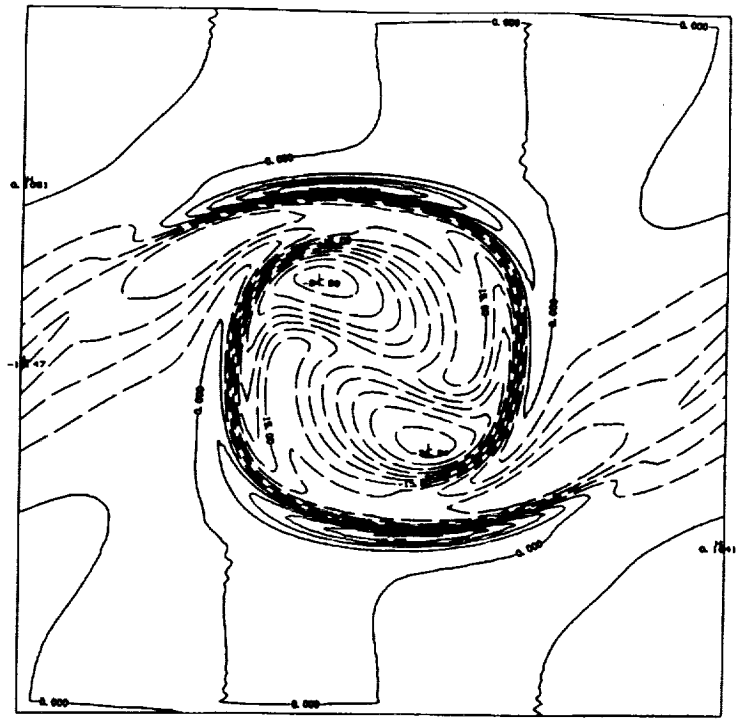

Figure 52: Plot of vorticity contours for $\epsilon_1 = \epsilon_2 = 0.005$ at time $t^* = 2.1$.

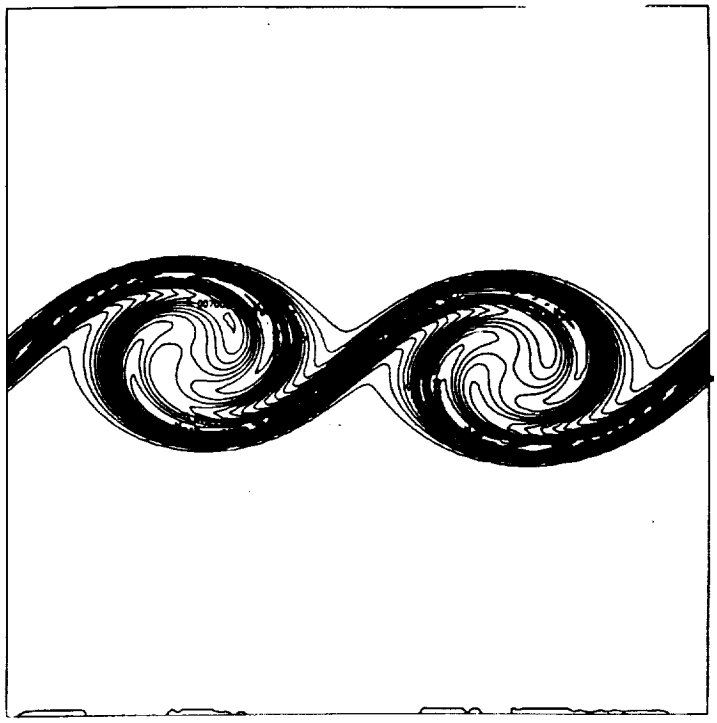

Figure 53: Plot of reaction rate contours, $Ze = 20$, $t^* = 1$.

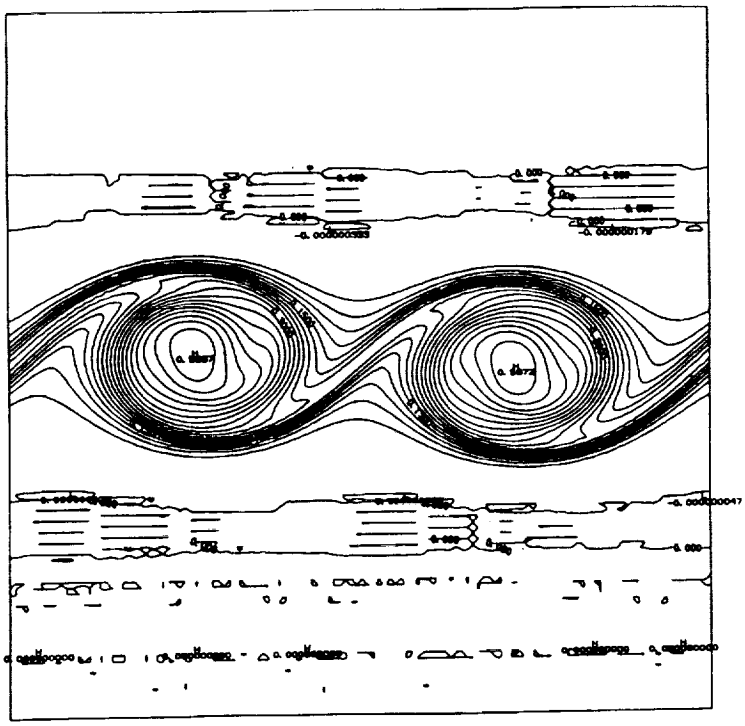

Figure 54: Plot of product concentration contours, $Ze = 20$, $t^* = 1$.

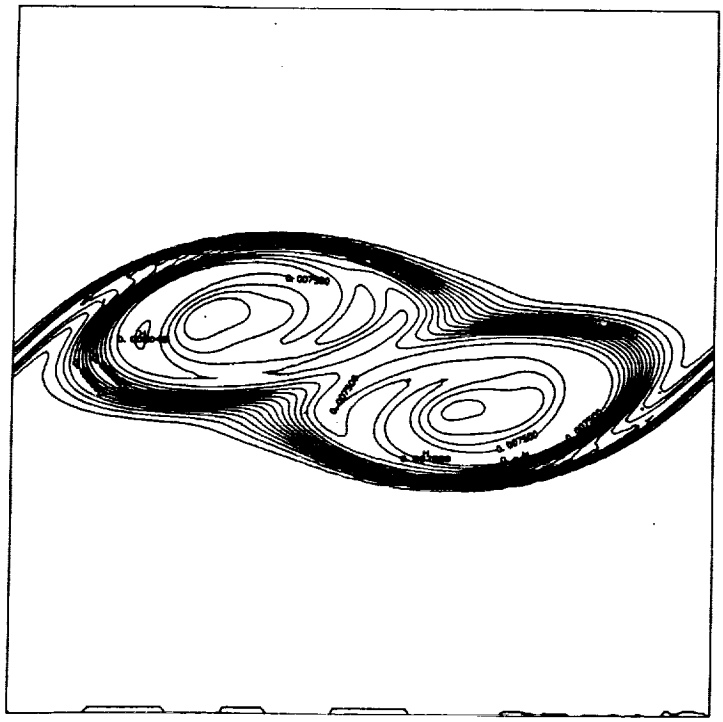

Figure 55: Plot of reaction rate contours, $Ze = 20$, $t^* = 1.5$.

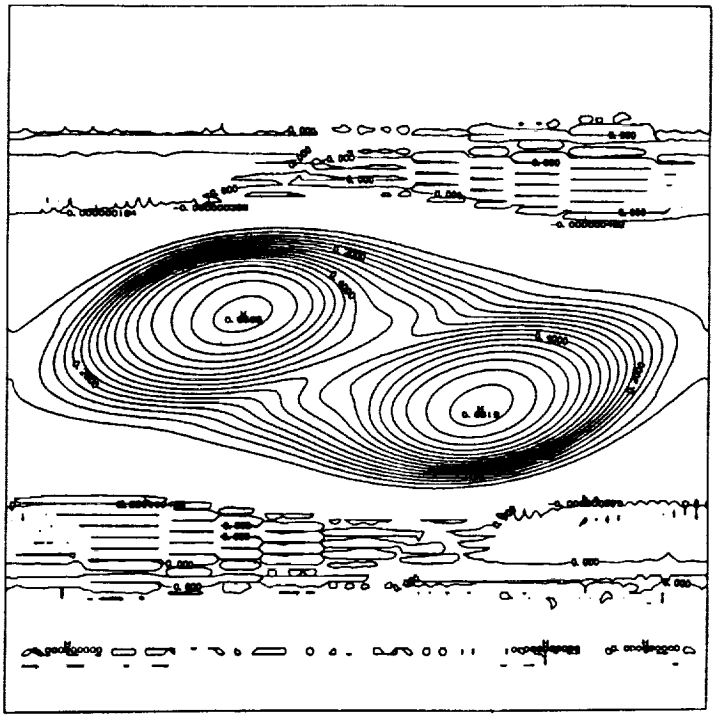

Figure 56: Plot of product concentration contours, $Ze = 20$, $t^* = 1.5$.

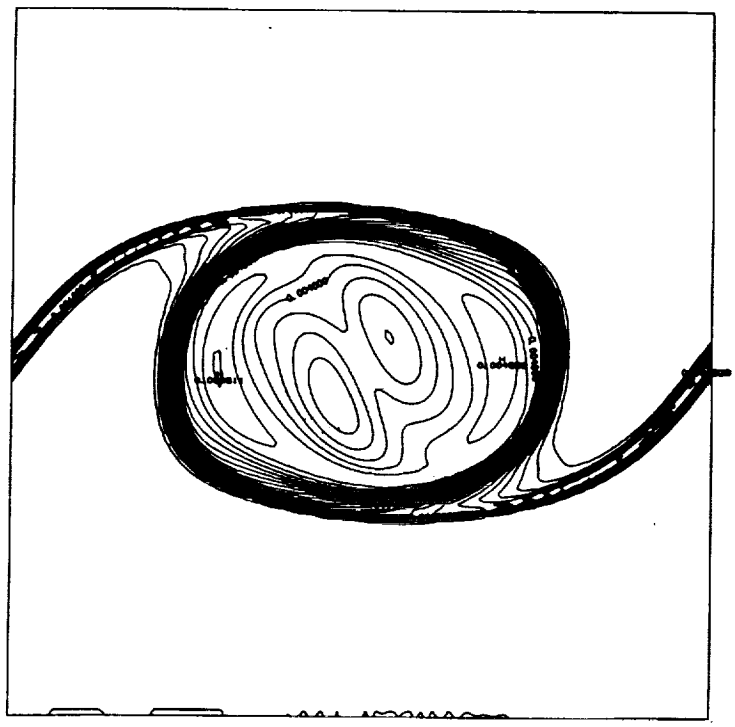

Figure 57: Plot of reaction rate contours, $Ze = 20$, $t^* = 2.25$.

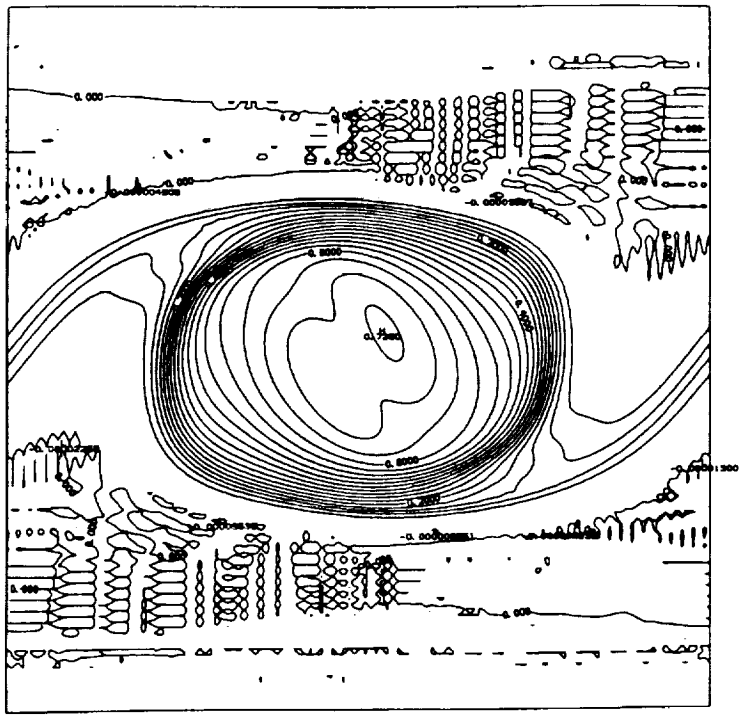

Figure 58: Plot of product concentration contours, $Ze = 20$, $t^* = 2.25$.

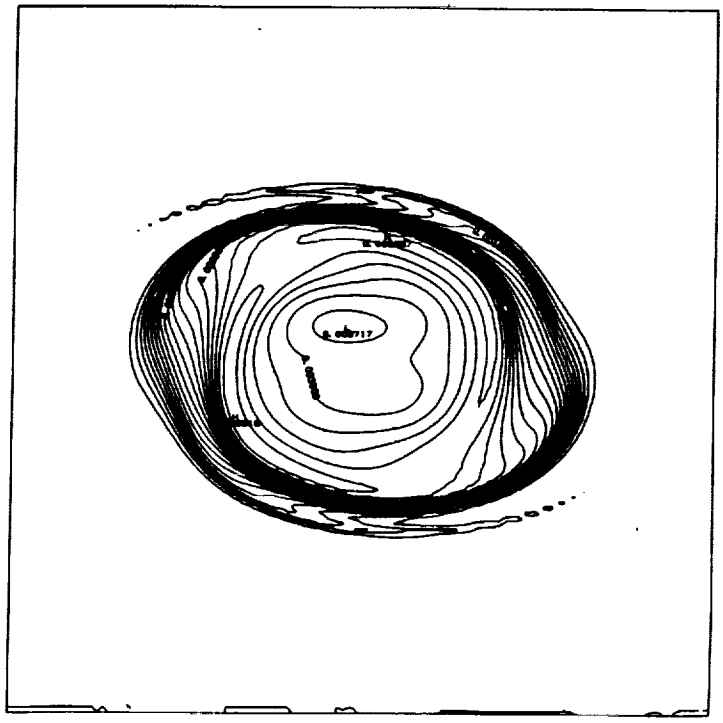

Figure 59: Plot of reaction rate contours, $Ze = 20$, $t^* = 2.5$.

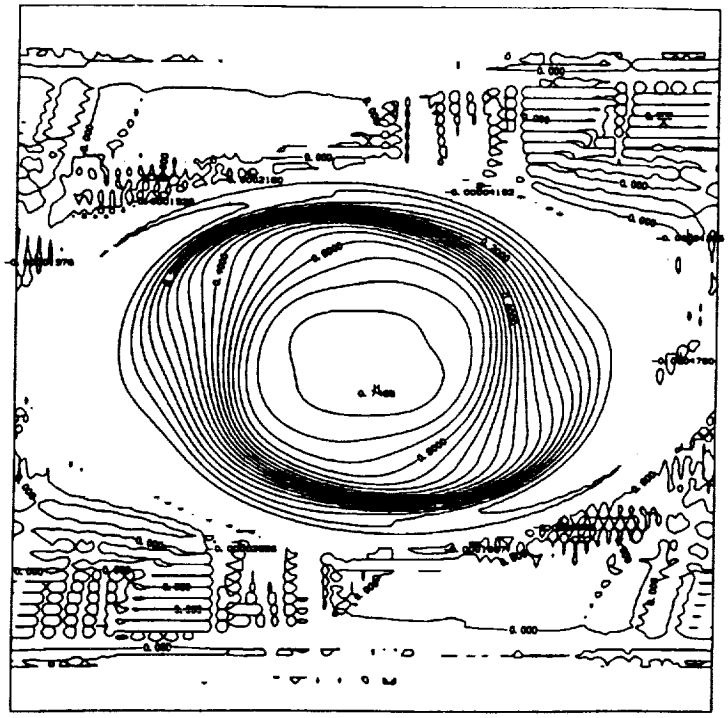

Figure 60: Plot of product concentration contours, $Ze = 20$, $t^* = 2.5$.

NASA
National Aeronautics and Space Administration

Report Documentation Page

1. Report No.	2. Government Accession No.	3. Recipient's Catalog No.
NASA CR -187084		

4. Title and Subtitle
Mixing and Non-Equilibrium Chemical Reaction in a Compressible Mixing Layer

5. Report Date
May 1991

6. Performing Organization Code

7. Author(s)
Craig J. Steinberger

8. Performing Organization Report No.
None

10. Work Unit No.
537-02-20

9. Performing Organization Name and Address
State University of New York at Buffalo
Department of Mechanical and Aerospace Engineering
Buffalo, New York 14222

11. Contract or Grant No.
NAG3-1011 and NAG1-1122

13. Type of Report and Period Covered
Contractor Report
Final

12. Sponsoring Agency Name and Address
National Aeronautics and Space Administration
Lewis Research Center
Cleveland, Ohio 44135 - 3191

14. Sponsoring Agency Code

15. Supplementary Notes
Project Manager, James D. Holdeman, Internal Fluid Mechanics Division, NASA Lewis Research Center, (216) 433-5846. Report was submitted as a thesis in partial fulfillment of the requirements for the degree Master of Science to the State University of New York at Buffalo, Buffalo, New York 14222. Partial funding by the American Chemical Society under Grant 22227-66.

16. Abstract

The effects of compressibility, chemical reaction exothermicity and non-equilibrium chemical modeling in a reacting plane mixing layer were investigated by means of two dimensional direct numerical simulations. The chemical reaction was irreversible and second order of the type $A + B \rightarrow Products + Heat$. The general governing fluid equations of a compressible reacting flow field were solved by means of high order finite difference methods. Physical effects were then determined by examining the response of the mixing layer to variation of the relevant non-dimensionalized parameters. The simulations show that increased compressibility generally results in a suppressed mixing, and consequently a reduced chemical reaction conversion rate. Reaction heat release was found to enhance mixing at the initial stages of the layer's growth, but had a stabilizing effect at later times. The increased stability manifested itself in the suppression or delay of the formation of large coherent structures within the flow. Calculations were performed for a constant rate chemical kinetics model and an Arrhenius type kinetics prototype. The choice of the model was shown to have an effect on the development of the flow. The Arrhenius model caused a greater temperature increase due to reaction than the constant kinetics model. This had the same effect as increasing the exothermicity of the reaction. Localized flame quenching was also observed when the Zeldovich number was relatively large.

17. Key Words (Suggested by Author(s))	18. Distribution Statement
Mixing layer Direct numerical simulation Compressibility	Unclassified - Unlimited Subject Category ~~24~~ 07

19. Security Classif. (of the report)	20. Security Classif. (of this page)	21. No. of pages	22. Price*
Unclassified	Unclassified	75	A04

NASA FORM 1626 OCT 86

*For sale by the National Technical Information Service, Springfield, Virginia 22161